Polyvinylpyrrolidone-induced size-dependent catalytic behavior of Fe sites on N-doped carbon substrate and mechanism conversion in Fenton-like oxidation reaction

Haoyue Li [a], Na Wang [a,*], Han Li [a], Ziqiu Ren [a], Wenjie Ma [c], Jun Li [a], Yunchen Du [b], Qun Xu [a,*]

[a] *Henan Institute of Advanced Technology, Zhengzhou University, Zhengzhou 450003, China*
[b] *MIIT Key Laboratory of Critical Materials Technology for New Energy Conversion and Storage, School of Chemistry and Chemical Engineering, Harbin Institute of Technology, Harbin 150001, China*
[c] *College of Textiles and Clothing, Yancheng Institute of Technology, Yancheng 224051, China*

ARTICLE INFO

ABSTRACT

Fe-based N-doped carbon catalysts (Fe/NC-XPVP) are synthesized through a solvent-free and one-step pyrolysis strategy, allowing for the control of Fe active center sizes and the morphology of carbon substrates. The variable-sized Fe active centers in Fe/NC-XPVP exhibit size-dependent catalytic behavior in peroxymonosulfate (PMS) activation reaction, which indicates that downsizing Fe particles to atomic level achieves performance improvement and mechanism transformation from radical to non-radical pathway. The optimal Fe/NC-1.0PVP catalyst can realize nearly 100.0 % of tetracycline degradation efficiency within 30 min. Density functional theory calculations demonstrate that the strong adsorption of PMS onto $Fe-N_4$ sites can promote the formation of catalyst/PMS* complexes and induce the occurrence of electron transfer process, which performs great resistance to complex water environments during PMS activation. This work gives valuable insights into the precise design and regulation of metal active sites on N-doped carbon materials and provides a promising catalyst for waste-water remediation.

1. Introduction

The ever-rising consumption of fossil fuels, industrial chemicals, pharmaceuticals, and personal care products has given rise to significant concerns, such as global climate fluctuation and water contamination. Developing high-efficient and clean technologies to comprehensively address the water pollution is of utmost urgency to ensure the ecological balance and human health [1–3]. Peroxymonosulfate (PMS)-based advanced oxidation technologies (AOTs) have received widespread attention due to their strong oxidation capacity and stability in handling various stubborn contaminants [4,5]. PMS molecules can be activated by multiple means, for instance, heat, light, alkali, ultrasound, and catalysis to generate reactive oxygen species (ROSs), such as sulfate radical ($SO_4\bullet^-$, $E^0 =2.5–3.1$ eV), hydroxyl radical (HO•, $E^0 =1.8–2.7$ eV) and superoxide radical ($O_2\bullet^-$, $E^0 =2.4$ eV) [6,7]. ROSs can oxidize and decompose organics into uninjurious substances, carbon dioxide and water through a radical oxidation pathway. Although the radical process exhibits excellent oxidation ability towards contaminants, the ubiquitous inorganic ions (e.g., CO_3^{2-}, HCO_3^- and Cl^-) and natural organic matters in water always consume the generated ROSs, leading to the depressed degradation of pollutants and generation of toxic by-products [8,9]. Recently, numerous studies have shown that carbon-based heterogeneous catalysts and some metal catalysts can induce a non-radical oxidation process, which depends on the formation of singlet oxygen ($^1O_2$) to oxidize organic pollutants [10–12]. In addition, electron transfer process and direct oxidative transfer process have also been widely studied as non-radical pathways owing to their technical advantages [13–15]. Compared to radical process, non-radical process presents highly-efficient selectivity to electron-rich pollutants and possesses incomparable resistance to complex water environments. In view of this, the rational design and regulation of catalyst to achieve performance improvement and mechanism transition from radical pathway to non-radical pathway in Fenton-like reaction is an attractive topic, while few relevant reports are available.

Transition metal-based carbon catalysts have been extensively reported as PMS activators with amazing catalytic ability to remove

---

organic pollutants through radical and non-radical oxidation processes, while the solidification of metal sites still remains, resulting in inadequate utilization of active centers and rapid deterioration of catalytic performance [16–18]. Therefore, it is particularly important to maximize the utilization of active sites and improve the mass transfer process in PMS activation reaction. Generally, the catalytic activity and kinetic behavior of the supported metal catalysts have a significant dependence on the metal particle size. From the perspective of geometric and electronic structures, in addition to high surface area, downsizing of metal particles is favorable for exposing more low-coordination atoms, thereby altering the structure and proportion of active centers on the surface of catalyst [19–21]. In addition, the energy levels of metal active centers can be modified appropriately due to quantum size effects that greatly influence the orbital hybridization and charge transfer between catalyst and reactant [22]. Furthermore, when the size of active metal component is engineered to be atomic level, the obtained catalysts with different metal center sizes will exhibit different electronic states, thereby imparting unique catalytic performance.

Single-atom catalysts (SACs) are emerging heterogeneous catalysts that exhibit extraordinary catalytic activity in PMS-AOTs due to their fully atom-utilization efficiency and adjustable electronic structures [23–27]. Many recent researches have proposed that the individual metal sites immobilized on carbon supports usually induce the formation of non-radical pathway during the activation of PMS [28–31]. For example, Xu and co-workers fabricated the atomically dispersed Fe on g-C_3N_4 to activate PMS to degrade *o*-phenylphenol. They found that the mediated electron transfer plays a dominant role in the degradation of organics [28]. Meng et al. compared PMS activation ability of Fe nanoparticles/biochar (nano-Fe/MC) and Fe single atoms/biochar (ISA-Fe/MC), and revealed that the electron transfer reigned non-radical pathway for ISAFe/MC because of the enhanced density of states and the promoted electron transfer between single-atom Fe and adjacent C and N [30]. Although many efforts have been devoted to improving the catalytic performance of SACs and investigating the non-radical mechanism of PMS activation reaction, few attentions are paid to systematically study the intrinsic relationship between the size of metal active sites and reaction mechanism. Developing effective means to tune the properties of catalyst, control the generation of active species, and thus inducing the formation of non-radical pathway is of great significance for water treatment.

In this work, a series of Fe-based N-doped carbon catalysts (Fe/NC-XPVP) with variable-sized Fe active centers are prepared by pyrolyzing a solid mixture consisting of $Fe(NO_3)_3 \cdot 9\ H_2O$, melamine, and polyvinylpyrrolidone (PVP). The size of Fe active centers and the morphology of carbon substrates can be regulated by varying PVP dosage in the precursor. The atomically dispersed Fe supported on carbon nanosheets can be achieved by this solvent-free and one-step strategy, which greatly simplifies the synthesis procedure of SACs. Tetracycline (TC) is selected as a model pollutant to evaluate the size-dependent catalytic behavior of Fe/NC-XPVP in PMS activation reaction. It is shown that downsizing Fe particles to atomic level leads to performance enhancement and reaction mechanism transformation. The cooperation of Fe nanoparticles/clusters and single atoms can boost the catalytic performance of Fe/NC-XPVP to some extent. The non-radical oxidation mechanism ($^1O_2$ and electron transfer) of TC degradation at Fe-N_4 sites is proposed based on experimental results and theoretical analysis. DFT calculations demonstrate that the strong adsorption of PMS on the surface of Fe-N_4 sites plays a critical role in promoting the formation of catalyst/PMS intermediate complexes and inducing the occurrence of electron transfer process. The effects of operational parameters and co-existing anions on TC removal are investigated, and the results indicate that the Fe-N_4/PMS system exhibits great resistance to complicated water environments.

2. Experimental section

2.1. Chemicals

Tetracycline (TC), sulfamethoxazole (SMX), and *p*-Nitrophenol (*p*-NP) were provided by Shanghai Macklin Biochemical Co., Ltd. Methanol (MeOH), polyvinylpyrrolidone (PVP), sodium thiosulphate ($Na_2S_2O_3 \cdot 5\ H_2O$), sodium bicarbonate ($NaHCO_3$), sodium nitrate ($NaNO_3$), sodium chloride (NaCl), sodium dihydrogen phosphate ($NaH_2PO_4 \cdot 2\ H_2O$), sodium sulfate (Na_2SO_4), ethanol (EtOH), Potassium thiocyanate (KSCN), and oxalate ($C_2H_2O_4 \cdot 2\ H_2O$) were obtained from Sinopharm Chemical Reagent Co., Ltd. Melamine, *p*-Benzoquinone (*p*-BQ), 2,2,6,6-tetramethyl-4-piperidinyloxyl (TEMP), 5,5-dimethyl-1-pyrroline N-oxide (DMPO), peroxymonosulfate (PMS), chloroform ($CHCl_3$), sodium hydroxide (NaOH), sulfuric acid (H_2SO_4), Iron (III) nitrate nonahydrate ($Fe(NO_3)_3 \cdot 9\ H_2O$), L-histidine, Nafion, Rhodamine B (RhB), and Ferrous chloride tetrahydrate ($FeCl_2 \cdot 4\ H_2O$) were purchased from Shanghai Aladdin Biochemical Technology Co., Ltd.

2.2. Synthesis of Fe/NC-XPVP

In this work, Fe/NC-XPVP catalysts were synthesized by a simple one-step pyrolysis method according to our previous work with some modifications [32]. Briefly, 0.2 g of $Fe(NO_3)_3 \cdot 9\ H_2O$, 12 g of melamine, and a certain amount of PVP (0, 0.05, 0.5, 1.0, 2.0, and 4.0 g) were mixed and ground into a homogeneous powder in an agate mortar. Then, the obtained fine powder mixture was transferred into a tubular furnace and pyrolyzed in argon atmosphere. Specifically, the pyrolysis temperature was increased from 25 °C to 600 °C with a heating rate of 3 °C min^{-1}, and maintained for 2 h. Then, the temperature was increased from 600 °C to 900 °C with a ramping rate of 2 °C min^{-1}, and maintained for 1 h. After cooling to room temperature, a series of Fe/NC-XPVP (X = 0, 0.05, 0.5, 1.0, 2.0, and 4.0) were obtained for subsequent experiments.

2.3. Characterizations

Transmission electron microscopy (TEM) images were taken on a JEM 2100 F (JEOL JPN). The high-angle annular dark-field scanning transmission electron microscopy (HAADF-STEM) was obtained on a JEOL JEM-ARM300F with a spherical aberration corrector. Scanning electron microscopy (SEM) images were recorded by a Sigma 300 (ZEISS, GER). Nitrogen adsorption-desorption isotherms were recorded on an ASAP 2460 (Micromeritics, USA). Degassing condition of samples are 200 °C for 10 h. Brunauer-Emmett-Teller (BET) surface area was evaluated by the adsorption data. X-ray photoelectron spectroscopy (XPS) was measured on an ESCALAB 250XI (Thermo, USA) using Al Kα as the excitation source. Powder X-ray diffraction (XRD) patterns were taken on a Rigaku D/Max 2550 X-ray diffractometer with Cu Kα radiation (λ = 1.5418 Å). Fourier transform infrared (FTIR) spectra were obtained using a Bruker INVENIO spectrometer. UV–vis–NIR spectra were collected to evaluate the light adsorption of pollutant using Shimadzu UV-3600 Plus UV/Vis-NIR spectrometer. Raman spectra were recorded on LabRAM HR Evolution Raman spectrometer. Total organic carbon (TOC) analysis was performed on a Shimadzu TOC-L analyzer. The intermediate products and degradation pathway of TC were analyzed using liquid chromatography-mass spectrometer (LC-MS, Ultimate 3000 UHPLC-Q). The content of Fe of the catalysts was measured by inductively coupled plasma optical emission spectroscopy (ICP-OES) conducted on Agilent 5800. The Fe ion leakage was evaluated by inductively coupled plasma-mass spectrometry (ICP-MS) conducted on Agilent 7800. X-ray absorption near-edge structure (XANES) and extended X-ray absorption fine structure (EXAFS) measurements were measured on the National Synchrotron Radiation Research Center (NSRRC) of Taiwan.

2.4. Experimental procedures

TC was utilized as a model pollutant to evaluate PMS activation performance of Fe/NC-XPVP. All degradation experiments were performed in a 100 mL beaker at room temperature (20 °C). The temperature-controlled experiments (25, 35, and 45 °C) were performed in a constant-temperature water bath. In a typical process, 5 mg of catalyst was dispersed into 50 mL of TC solution (20 ppm) by magnetic stirring and the obtained solution was stirred for 20 min to achieve adsorption-desorption equilibrium. Subsequently, the oxidation reaction was triggered by adding a certain amount of PMS. During the degradation of TC, 1.0 mL reaction solution was withdrawn at certain intervals quickly, filtered through 0.22 μm of filter membrane, and quenched by saturated sodium thiosulfate solution. pH value of the reaction solution was adjusted by NaOH and H_2SO_4 solution. The concentration of extracted pollutants was measured by UV–vis spectroscopy. The used catalyst was collected after reaction by centrifugation, washed and calcinated at 300 °C for 2 h in air to remove the oxidized functional groups on the surface of catalyst for reuse. The degradation efficiency of TC could be calculated by the following equation:

$$\text{Degradation efficiency of TC (\%)} = [(TC_0 - TC_t)/TC_0] \times 100\ \% \quad (1)$$

The reaction rate constants (k_{obs}) of TC degradation under different conditions were evaluated by the pseudo-first-order kinetics model:

$$-\ln([TC_t]/[TC_0]) = k_{obs} \times t \quad (2)$$

where $[TC_t]$ was the concentration of TC at a certain reaction time (t) and $[TC_0]$ represented the initial concentration of TC solution. Arrhenius equation was used to calculate the activation energy of TC degradation:

$$\ln k_{obs} = \ln A - E_a/RT \quad (3)$$

where A standed for pre-exponential factor (min^{-1}), E_a represented activation energy (kJ mol^{-1}), R was the universal gas constant (8.314 J $\text{mol}^{-1}\ \text{K}^{-1}$), and T was the reaction temperature (K).

2.5. Electrochemical measurements

All electrochemical measurements were performed using an electrochemical workstation (CHI 760E) with a three-electrode configuration with Ag/AgCl and platinum plate electrodes as reference and counter electrodes, respectively. The working electrode was prepared by mixing 1 mL of ethanol, 20 μL of Nafion and 5 mg of catalyst and sonicating for 40 min to form a black and homogeneous suspension. Then, 200 μL of suspension was deposited on a carbon paper (1 $\times$1 cm^2) and dried naturally. 40 mL of 100 mM Na_2SO_4 solution was used as electrolyte. The electrochemical impedance spectrum (EIS) of the working electrode was measured at 1 Hz $\sim$ 0.1 MHz.

2.6. DFT calculations

The first-principles [33] have been employed to perform all density functional theory (DFT) calculations within the generalized gradient approximation (GGA) using the Perdew-Burke-Ernzerhof (PBE) formulation [34]. We have chosen the projected augmented wave (PAW) potentials to describe the ionic cores and taken valence electrons into account using a plane wave basis set with a kinetic energy cutoff of 520 eV [35,36]. Partial occupancies of the Kohn−Sham orbitals were allowed using the Gaussian smearing method with the width of 0.05 eV. The electronic energy was considered self-consistent when the energy change was smaller than 10^{-6} eV. A geometry optimization was considered convergent when the energy change was smaller than 0.05 eV Å^{-1}. The vacuum spacing in a direction perpendicular to the plane of the structure was 20 Å for the surfaces. The Brillouin zone integration

was performed using 2 $\times$ 2 $\times$ 1 Monkhorst-Pack k-point sampling for a structure. Finally, the adsorption energies (E_{ads}) were calculated by Eq. (4):

$$E_{ads} = E_{ad/sub} - E_{ad} - E_{sub} \quad (4)$$

where $E_{ad/sub}$, E_{ad}, and E_{sub} were the total energies of the optimized adsorbate/substrate system, the adsorbate in the structure, and the clean substrate, respectively.

3. Results and discussion

3.1. Characteristics of Fe/NC-XPVP

Fe-based N-doped carbon catalysts (Fe/NC-XPVP) with variable-sized Fe active centers are prepared by pyrolyzing a homogeneous mixture composed of $Fe(NO_3)_3$•9 H_2O, melamine, and PVP. The synthesis procedure is schematically illustrated in Fig. 1a. During the thermal treatment, melamine will be preliminarily converted to graphitic carbon nitride (g-C_3N_4) under the high-temperature treatment (above 400 °C) in Ar atmosphere. PVP is utilized as surface stabilizer and nanoparticle dispersant to inhibit the self-aggregation of Fe nanoparticles via the strong repulsive forces that arise from the interaction between hydrophobic carbon chains (steric-hindrance effect) [37]. Additionally, the repeating carbonyl groups (C=O) and nitrogen atoms of pyrrolidone ring in PVP molecule can contribute lone pairs of electrons to Fe ions, resulting in strong interactions with Fe sites and promoting the dispersion of Fe on carbon substrates [38]. To get a deeper insight into the role of PVP in the preparation of Fe/NC-XPVP, two objects, Fe/NC-0PVP and Fe/NC-1.0PVP obtained at different pyrolysis temperatures, are investigated in detail. FTIR spectra indicate that Fe/NC-0PVP-600 and Fe/NC-1.0PVP-600 display almost identical absorption signals (Fig. S1a). The sharp peak at 810 cm^{-1} is attributed to the breathing mode of triazine rings. The typical signals centered at 1200–1700 cm^{-1} are assigned to the stretching mode of C-N heterocycles. The bands at 3100–3500 cm^{-1} correspond to the stretching mode of N-H and adsorbed hydroxyl species [39]. These observations demonstrate that melamine is turned into g-C_3N_4 at 600 °C. The generated g-C_3N_4 serves as two-dimensional template to support the distribution of Fe nanoparticles. g-C_3N_4 in Fe/NC-0PVP-700 is thermally decomposed and converted to N-doped carbon at 700 °C (Fig. S1b). In contrast, Fe/NC-1.0PVP-700 can still maintain some carbon nitride structures thanks to the stabilization effect of PVP. A similar phenomenon is observed in Fe/NC-1.0PVP-800 and Fe/NC-1.0PVP-900 (Fe/NC-1.0PVP) (Fig. S1c and d). It can be seen that the presence of PVP is beneficial to enhancing the stability of g-C_3N_4-like structures under the high-temperature treatment. XRD measurements are further performed to verify above findings (Fig. S2). Fe/NC-0PVP-600 and Fe/NC-1.0PVP-600 give similar diffraction peaks attributed to g-C_3N_4, in agreement with the results of FTIR spectra. The diffraction peaks of metallic Fe species are not observed in Fe/NC-1.0PVP obtained at different temperatures, but the typical signals of Fe species are always detected in Fe/NC-0PVP-700, Fe/NC-0PVP-800 and Fe/NC-0PVP-900. This suggests that PVP can effectively prevent the aggregation of Fe nanoparticles and promote the dispersion of Fe species during the thermal treatment.

The morphology and microstructure of Fe/NC-XPVP are evaluated by SEM and TEM images. As shown in Fig. 1b, Fe/NC-0PVP shows one-dimensional bamboo-like carbon nanotubes with many encapsulated Fe nanoparticles, the size of which is distributed between 50 and 200 nm (Fig. 1g). The graphitic-like carbon nanotubes are generated by the catalytic graphitization of Fe nanoparticles. This situation is further confirmed by SEM image (Fig. S3a) and the magnified TEM images (Fig. S4). TEM image of Fe/NC-0.05PVP indicates that Fe nanoparticle size decreases significantly when 0.05 g of PVP is added in the precursor (Fig. 1c), and the size distribution of Fe nanoparticles is located at
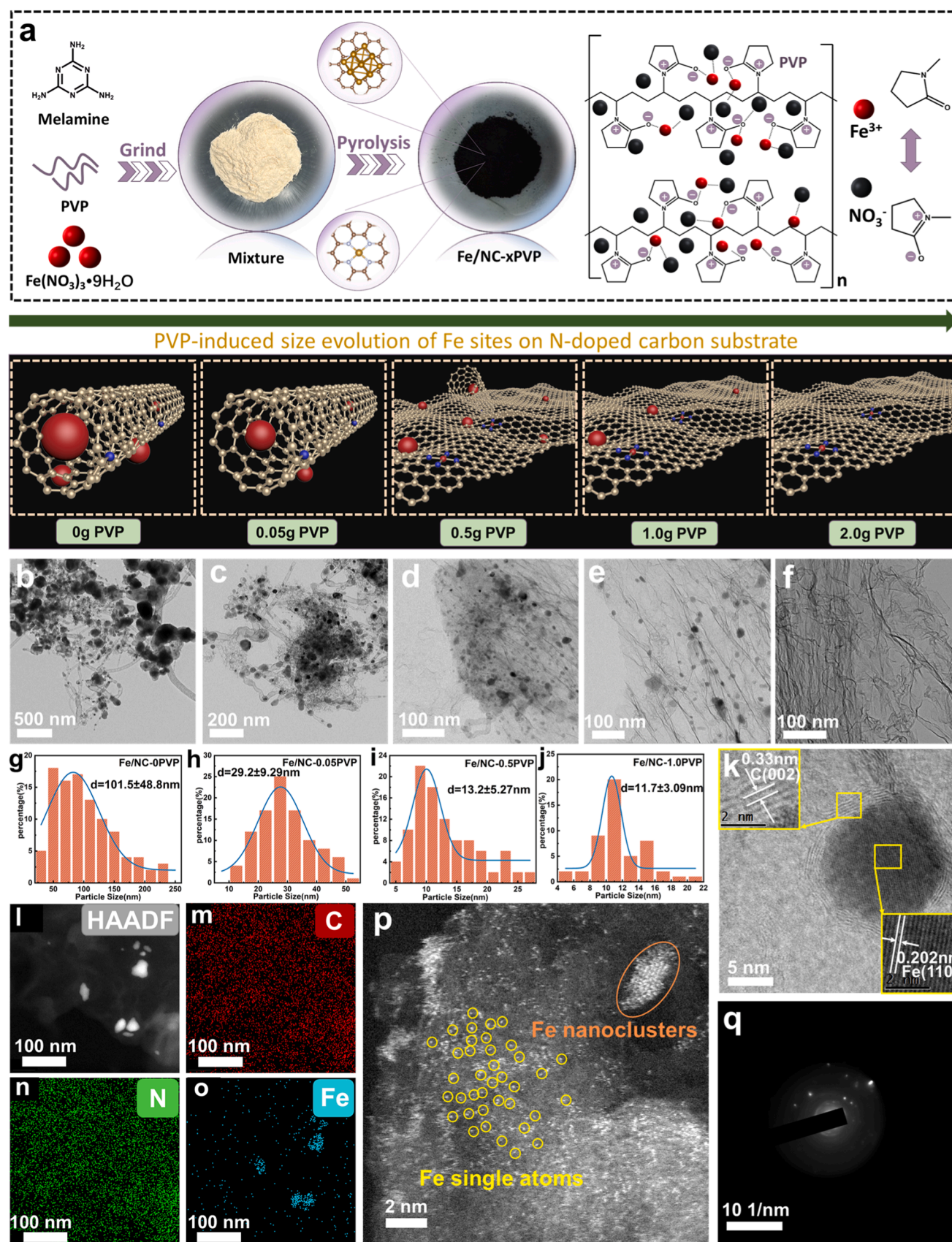
Fig. 1. (a) Schematic illustration of the preparation of Fe/NC-XPVP; TEM images of (b) Fe/NC-0PVP, (c) Fe/NC-0.05PVP, (d) Fe/NC-0.5PVP, (e) Fe/NC-1.0PVP, and (f) Fe/NC-2.0PVP; (g-j) the size distribution of Fe species in Fe/NC-0PVP, Fe/NC-0.05PVP, Fe/NC-0.5PVP, and Fe/NC-1.0PVP; (k) HRTEM image of Fe/NC-1.0PVP and (q) the corresponding SAED pattern; (l-o) EDS mappings and (p) magnified HAADF-STEM image of Fe/NC-1.0PVP.

20–40 nm (Fig. 1h), which corroborates the decisive role of PVP in inhibiting the aggregation of Fe species. The amount of recognizable Fe nanoparticles in Fe/NC-0.5PVP and Fe/NC-1.0PVP is further reduced by increasing the dosage of PVP in the precursor (Fig. 1d and e), and the particle size of Fe is also suppressed to below 20 nm (Fig. 1i and j). In addition, it is noteworthy that the carbon nanotubes gradually disappear in Fe/NC-0.5PVP, Fe/NC-1.0PVP, and Fe/NC-2.0PVP, instead forming thin graphene-like carbon nanosheets (Fig. S3). This may be because smaller Fe nanoparticles and nanoclusters cannot catalyze the formation of carbon nanotubes under the stabilization effect of PVP. When the dosage of PVP is increased to 2.0 g, no obvious Fe nanoparticles are observed in Fe/NC-2.0PVP (Fig. 1f), suggesting that the dispersion degree of Fe on carbon matrix is definitely promoted by increasing PVP addition in the precursor. High-resolution TEM image of Fe/NC-1.0PVP is provided in Fig. 1k. A small individual Fe nanoparticle is observed to be encased in carbon layers. The disordered lattices with the interplanar spacing of 0.33 nm are attributed to the (002) plane of carbon, and the D-spacing of 0.202 nm corresponds to the (110) plane of Fe nanoparticles [40,41]. The elemental mapping images exhibit the distribution of Fe, C, and N elements in Fe/NC-1.0PVP (Fig. 1l-o), confirming the successful doping of N in carbon frameworks. The doped N atoms can trap and bond with Fe atoms to form Fe-N-C modes, which inhibit the aggregation of Fe nanoparticles and regulate the electronic structures of Fe active sites. The formation of Fe nanoclusters and single atoms on carbon nanosheets is identified by aberration-corrected high-angle annular dark field scanning transmission electron microscopy (HAADF-STEM) (Fig. 1p). The isolated bright spots can be clearly identified in Fe/NC-1.0PVP, illustrating the high dispersion of Fe atoms on the N-doped carbon substrates. Selected area electron diffraction (SAED) image in Fig. 1q presents the diffraction rings belonging to the low-crystallinity carbon nanosheets.

XRD patterns of Fe/NC-XPVP are provided in Fig. 2a. All samples present similar broad and sharp diffraction peaks at $2\theta = 26.3°$,

corresponding to (002) plane of graphite-like carbon with an interlayer spacing of 0.33 nm. The characteristic signals at $2\theta = 44.6°$, 65.0°, and 82.3° in Fe/NC-0PVP are precisely indexed to (110), (200), and (211) planes of zero-valent Fe (JCPDS #06–0696). In addition, some typical signals derived from Fe_3C (JCPDS #35–0772) are also collected, indicating the formation of Fe_3C phase in Fe/NC-0PVP. The signals belonging to metallic Fe and Fe_3C in Fe/NC-XPVP gradually weaken with the increase of PVP content in the precursor, which is consistent with TEM observation. Raman spectra demonstrate the typical carbon features of Fe/NC-XPVP, as indicated in Fig. 2b. The intensity ratio of D band (1350 cm^{-1}) to G band (1580 cm^{-1}) (I_D/I_G) can be utilized to evaluate the defect state of samples [42]. In general, D band represents the defects in sp^2 hybridized hexagonal lattice, and G band corresponds to the degree of graphitization [43]. Apparently, I_D/I_G values increase from 0.679 for Fe/NC-0PVP to 1.020 for Fe/NC-2.0PVP, illustrating that the structural distortion of carbon substrate of Fe/NC-XPVP is gradually increased. The increase in defect density of catalyst is beneficial to optimizing the adsorption capacity and adjusting the electronic structures of the catalyst surface.

The surface composition and chemical states of Fe/NC-XPVP are investigated by XPS. The survey spectra present the peaks assigned to C, N, Fe, and O elements, indicating the existence of Fe and N in carbon substrates (Fig. S5). The atomic concentration of each element is listed in Table S1. High-resolution Fe2p XPS spectra of Fe/NC-XPVP and the corresponding fitting results are displayed in Fig. 2c and Table S2. Fe/NC-0PVP gives two major peaks that can be separated into three parts, representing three oxidation states of Fe (Fe^0, Fe^{2+}, and Fe^{3+}). The signals centered at 707.0 and 720.1 eV are assigned to Fe^0 derived from Fe nanoparticles in Fe/NC-0PVP. The peaks located at 709.2 and 723.1 eV are attributed to Fe^{2+}, and the peaks at 712.5 and 725.6 eV are ascribed to Fe^{3+} [44,45]. The signals of Fe^0 can also be detected in Fe/NC-0.05PVP due to insufficient PVP dosage. Nevertheless, the proportion of Fe^0 on the surface of Fe/NC-0.05PVP (20.72 %) is lower than
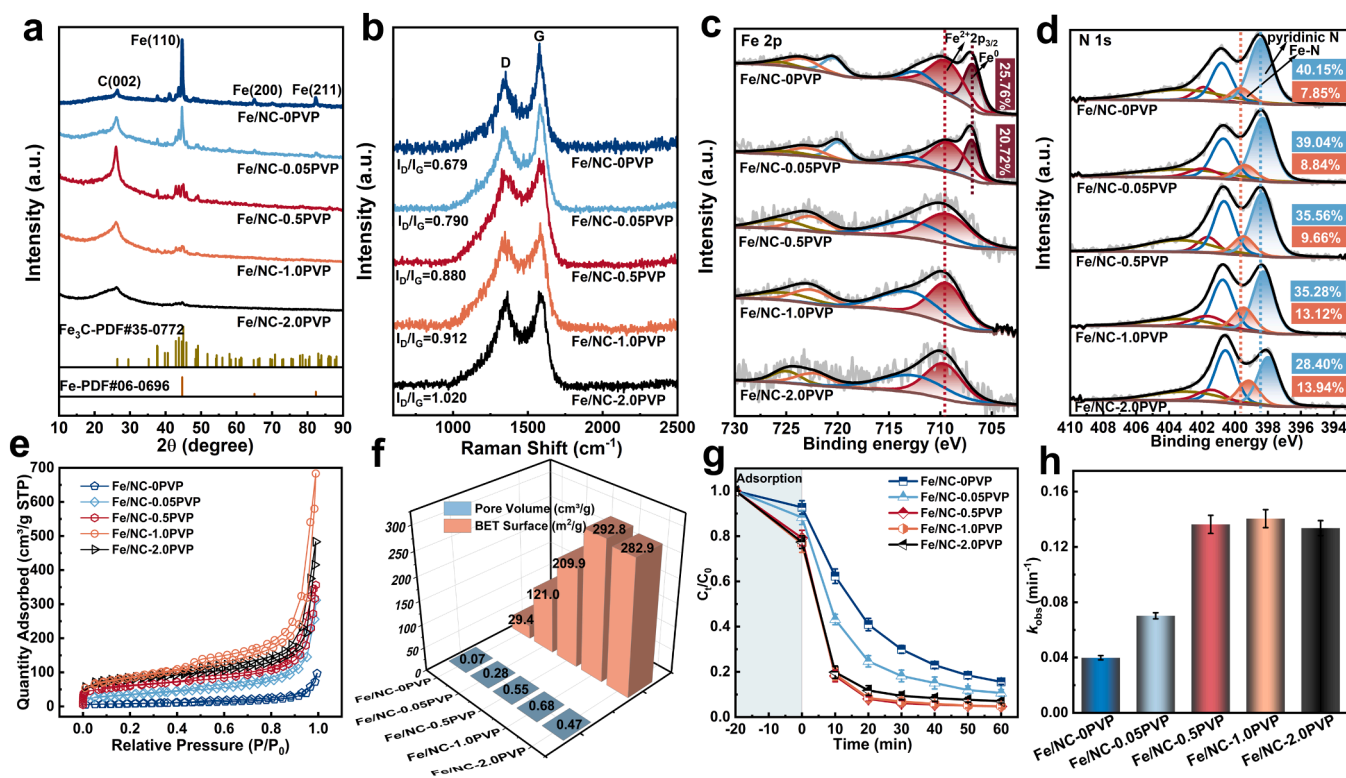

Fig. 2. (a) XRD patterns, (b) Raman spectra, high-resolution XPS spectra of (c) Fe 2p and (d) N 1 s of Fe/NC-XPVP; (e) N_2 adsorption-desorption isotherms and (f) the corresponding pore volumes of Fe/NC-XPVP; (g) TC degradation efficiency and (h) the corresponding reaction rate constants in Fe/NC-XPVP/PMS systems (TC: 20 mg/L, PMS: 1000 mg/L, catalyst: 0.1 g/L, T = 20 °C, and pH = 6).

that of Fe/NC-0PVP (25.76 %). It can be seen that the aggregation of Fe species in Fe/NC-XPVP can be inhibited by increasing the amount of PVP. The absence of Fe^0 signals in Fe/NC-0.5PVP, Fe/NC-1.0PVP, and Fe/NC-2.0PVP further proves the rationality of this conclusion. High-resolution N1s spectra of Fe/NC-XPVP reveal the presence of five types of N in all samples, namely pyridinic N (398.3 eV), pyrrolic N (400.7 eV), Fe-N (399.6 eV), graphitic N (401.8 eV) and oxidized N (403.2 eV) (Fig. 2d) [44]. The content of N in different configurations is shown in Table S3. The content of Fe-N on the surface of Fe/NC-XPVP increases gradually with the increase of PVP dosage, demonstrating that more Fe-N-C configurations are formed due to dispersion effect of PVP. In addition, it is also noted that the content of pyridinic N on the surface of Fe/NC-XPVP exhibits a gradual decline. This observation means that pyridinic N provides coordination sites to Fe atoms in the form of $Fe-N_x$ configuration in Fe/NC-XPVP. The slight chemical shift of pyridinic N to lower binding energy also corroborates this speculation [46,47]. XANES and EXAFS spectra are applied to prove the presence of $Fe-N_x$ configuration in Fe/NC-1.0PVP. The adsorption edge of Fe/NC-1.0PVP is located at a higher photon energy than that of Fe foil (Fe^0) but is lower than that of Fe_2O_3 (Fe^{3+}), manifesting that the average oxidation state of Fe in Fe/NC-1.0PVP is between 0 and + 3 (Fig. S6a). The Fourier transformed k^3-weighted EXAFS spectra identify the coordination configuration of Fe/NC-1.0PVP (Fig. S6b). Fe/NC-1.0PVP shows the major peak at 2.2 Å corresponding to the Fe-Fe structure of Fe nanoparticles. Another peak at 1.4 Å is ascribed to the Fe-N bonds, demonstrating the presence of Fe single atoms in Fe/NC-1.0PVP. The EXAFS fitting parameters show that the Fe-N coordination number is 3.8 (Table S4), confirming the $Fe-N_4$ structure in Fe/NC-1.0PVP similar to phthalocyanine (Pc). The wavelet transformed (WT) plots of different samples are indicated in Fig. S6c-f. Fe/NC-1.0PVP presents the WT at 7.5 and 4.2 $Å^{-1}$, respectively, assigning to the Fe-Fe and Fe-N bondings as compared with Fe foil and FePc.

3.2. The adsorption and catalytic performance of Fe/NC-XPVP

High specific surface area and porosity of heterogeneous catalyst can contribute to enriching the active sites per mass of the catalyst, creating more opportunities for the reaction substrates to access the catalyst surface, thereby enhancing the reaction rate to some extent. N_2 adsorption-desorption measurement is employed to evaluate the pore structure properties of Fe/NC-XPVP. As shown in Fig. 2e, all samples exhibit type-IV isotherm with H1 hysteresis loop at a relatively high pressure of $1.0 > P/P_0 > 0.5$, which is ascribed to the presence of mesoporous structure in Fe/NC-XPVP [44]. BET surface areas of Fe/NC-0PVP, Fe/NC-0.05PVP, Fe/NC-0.5PVP, Fe/NC-1.0PVP, and Fe/NC-2.0PVP are calculated to be 29.4, 121.0, 209.9, 292.8, and 282.9 m^2 g^{-1}, and the pore volumes are determined to be 0.07, 0.28, 0.55, 0.68 and 0.47 cm^3 g^{-1}, respectively (Fig. 2f). The pore size distribution data suggest that Fe/NC-XPVP catalysts exhibit similar mesoporous structure, which is conducive to promoting the mass transfer and electron transport processes during the catalytic reaction (Fig. S7). Apparently, PVP plays a positive role in dispersing Fe nanoparticles and stabilizing ultrathin carbon nanosheets to improve BET surface area and porosity of Fe/NC-XPVP when the amount of PVP is increased from 0 to 1.0 g. The slight decrease in BET surface area of Fe/NC-2.0PVP may be attributed to the close packing of carbon nanosheets under high-temperature treatment. To comprehensively explore the effect of PVP dosage on the characteristics of Fe/NC-XPVP, Fe/NC-4.0PVP is further prepared by increasing the dosage of PVP to 4.0 g. A sharply decreased BET surface area (131.6 m^2 g^{-1}) of Fe/NC-4.0PVP is obtained, confirming the negative effect of excessive PVP on BET surface area of the catalysts. XRD, TEM and XPS techniques are performed to analyze the composition and microstructure of Fe/NC-4.0PVP. Compared with Fe/NC-1.0PVP and Fe/NC-2.0PVP, the characteristic peaks of metal phase in Fe/NC-4.0PVP almost disappear (Fig. S8). TEM image also confirms the absence of metal nanoparticles in Fe/NC-4.0PVP (Fig. S9).

High-resolution Fe 2p and N 1 s XPS spectra of Fe/NC-4.0PVP and the fitting parameters are displayed in Fig. S10 and Table S5. The results indicate that the proportion of Fe-N configuration on the surface of Fe/NC-4.0PVP (14.56 %) is higher than that of Fe/NC-1.0PVP (13.12 %) and Fe/NC-2.0PVP (13.94 %). Although these findings can serve as evidence to prove that it is achievable to harvest pure Fe single-atom catalyst by increasing the dosage of PVP in the precursor, the reduction of BET surface area may have adverse effects on the catalytic performance of catalyst.

The catalytic performance of Fe/NC-XPVP is evaluated by the degradation of TC in the presence of PMS. As shown in Fig. 2g, Fe/NC-XPVP catalysts with different Fe center sizes present size-dependent catalytic behavior in PMS activation reaction. The adsorption ability of Fe/NC-0PVP for TC is very weak because of its small BET surface area and the agglomeration of Fe particles. Only 37.7 % of TC can be removed by Fe/NC-0PVP within 10 min, and the degradation efficiency of TC within 60 min is just 84.4 %. In contrast, Fe/NC-0.5PVP, Fe/NC-1.0PVP, and Fe/NC-2.0PVP exhibit highly efficient PMS activation activity. Especially, Fe/NC-1.0PVP can degrade 81.1 % of TC within 10 min and achieve almost 100.0 % of degradation efficiency within 30 min. Moreover, Fe/NC-1.0PVP has more significant advantages in TC degradation as compared with some previously reported catalysts (Table S6). The pseudo-first-order kinetics rate constants (k_{obs}) of TC degradation in Fe/NC-0PVP/PMS, Fe/NC-0.05PVP/PMS, Fe/NC-0.5PVP/PMS, Fe/NC-1.0PVP/PMS, and Fe/NC-2.0PVP/PMS systems are 0.040 min^{-1}, 0.070 min^{-1}, 0.136 min^{-1}, 0.140 min^{-1}, and 0.134 min^{-1}, respectively (Figs. 2h and S11). On the whole, the catalytic performance of Fe/NC-XPVP is rapidly improved when Fe particles supported on carbon nanotubes are converted to Fe nanoclusters and single atoms loaded on carbon nanosheets. In fact, it is noted that the catalytic activity of Fe/NC-2.0PVP and Fe/NC-4.0PVP decreases slightly as compared with Fe/NC-1.0PVP. The similar result can also be obtained when high concentration of TC is used as a model pollutant (Fig. S12). Considering the possible causes of this phenomenon, the dominant role of BET surface area can be excluded. This is because BET surface area of Fe/NC-4.0PVP (131.6 m^2 g^{-1}) is half that of Fe/NC-2.0PVP (282.9 m^2 g^{-1}), while the removal efficiency of TC by Fe/NC-4.0PVP is still comparable to that of Fe/NC-2.0PVP. The relationship between BET surface area of Fe/NC-XPVP and the reaction rate constants of TC degradation in Fe/NC-XPVP/PMS systems is presented in Fig. S13. The sharp decrease in BET surface area of Fe/NC-4.0PVP does not result in obvious depression of the catalytic performance, certifying that BET surface area is not the main factor determining the performance of catalyst. The degradation efficiency of TC by N-doped carbon nanosheets (NC) also confirms this speculation (Fig. S14). Although NC presents better adsorption efficiency for TC than Fe/NC-1.0PVP, the catalytic activity of NC is still far inferior to that of Fe/NC-1.0PVP. This result also proves the fact that the highly efficient decomposition of TC in Fe/NC-1.0PVP/PMS system is mainly attributed to Fe active centers on the catalyst surface. Another important factor affecting the catalytic activity of catalyst, Fe loading amount of Fe/NC-XPVP, is determined by ICP-OES. The weight percentage of Fe in Fe/NC-0PVP, Fe/NC-0.05PVP, Fe/NC-0.5PVP, Fe/NC-1.0PVP, Fe/NC-2.0PVP, and Fe/NC-4.0PVP is 76.57 wt%, 44.54 wt%, 14.05 wt%, 9.73 wt%, 5.49 wt%, and 2.66 wt%, respectively (Table S7). Notably, the high dispersion of Fe atoms on carbon matrix leads to the reduction of Fe loading amount per mass of the catalyst. Combining ICP results with the removal efficiency of TC by various catalysts (Fig. S15), it can be found that there is no obvious positive correlation between the degradation efficiency of TC and Fe loading amount of the catalysts. It is thus clear that the effect of Fe loading on the catalytic performance of Fe/NC-XPVP is relatively weak.

The above results demonstrate that the catalytic activity of Fe/NC-XPVP is closely related to the dispersion degree and chemical states of Fe active centers. The main reason for the slight performance decline of Fe/NC-2.0PVP and Fe/NC-4.0PVP may be the absence of Fe nanoparticles on carbon matrix. To examine this hypothesis, Fe/NC-1.0PVP is

treated with 1 M H_2SO_4 under the magnetic stirring for 6 h to remove Fe nanoparticles. XRD pattern illustrates that the peak intensity of Fe crystalline phases in the obtained sample (a-Fe/NC-1.0PVP) is weakened by acid treatment (Fig. S16a). TEM image also confirms the removal of most Fe nanoparticles from Fe/NC-1.0PVP (Fig. S16b). The degradation efficiency of TC by a-Fe/NC-1.0PVP shows a slight decrease due to the elimination of Fe nanoparticles (Fig. S17), implying that the presence of Fe nanoparticles plays a certain role in boosting the catalytic performance of Fe/NC-1.0PVP. The similar synergistic effect between metal nanoparticles and atomic sites has been also reported by previous works [48,49]. Based on these advanced researches, it can be inferred that the appropriate co-existence of Fe nanoparticles and Fe-N$_4$ sites on carbon matrix can optimize PMS activation activity of Fe/NC-XPVP catalysts. The dispersive Fe nanoparticles may act as an electronic bridge to regulate the electron density of Fe-N$_4$ sites and promote the electron transfer process between catalyst and oxidant. Nevertheless, the atomically dispersed Fe sites are still considered to be the main factor determining the rapid degradation of TC in Fe/NC-1.0PVP/PMS system. This can be further confirmed by the poison experiment that SCN$^-$ is adopted to poison Fe single sites on carbon matrix (Fig. S18). TC degradation is almost completely inhibited by SCN$^-$ addition, which is possibly attributed to the coverage of active Fe-N$_4$ sites by SCN$^-$ [32]. Therefore, combined results support the conclusion that the optimal catalytic performance of Fe/NC-1.0PVP is mainly due to the high dispersion and full utilization of atomic Fe-N$_4$ sites on carbon substrate. High BET surface area and the presence of Fe nanoparticles can help to synergistically improve the catalytic activity of the catalysts.

ICP-MS is utilized to detect the leaching concentration of Fe ion after the reaction (Table S8). The concentration of Fe ion in Fe/NC-0PVP/PMS system is 0.89 mg/L, which is 2.5 times that in Fe/NC-1.0PVP/PMS system (0.35 mg/L). The atomically dispersed Fe-N$_4$ sites exhibit higher stability than Fe particles in Fe/NC-0PVP during the oxidation reaction. The contribution of homogeneous catalysis to TC degradation in Fe/NC-1.0PVP/PMS system is considered by a simulated homogeneous experiment (Fig. S19). The degradation efficiency of TC in Fe^{2+}/PMS system can reach 63.4 % within 60 min, which is just slightly higher than that in sole PMS system. Moreover, the removal of TC by Fe^{2+} can be completely inhibited by MeOH addition. These results imply that the contribution of homogeneous catalysis induced by Fe ion leakage to TC removal in Fe/NC-1.0PVP/PMS system can be excluded. Additionally, the used concentration of Fe^{2+} is the total Fe ion concentration in the system after the reaction, and the real-time leakage of Fe ion is far less than this result. Thus, it is reasonable to infer that the homogeneous catalysis in the current system is negligible.

3.3. Investigation of reaction mechanism

3.3.1. Identification of active radicals
To ascertain the reaction mechanism of TC degradation, the primary c in Fe/NC-0PVP/PMS and Fe/NC-1.0PVP/PMS systems are explored by quenching experiments. Methanol (MeOH) is usually used to verify the presence of SO$_4$•$^-$ ($k = 3.2 \times 10^7$ M^{-1}·s^{-1}) and HO• ($k = 9.7 \times 10^8$ M^{-1}·s^{-1}) [50]. The degradation efficiency of TC in Fe/NC-0PVP/PMS system decreases from 84.4 % to 69.2 % in the presence of high levels
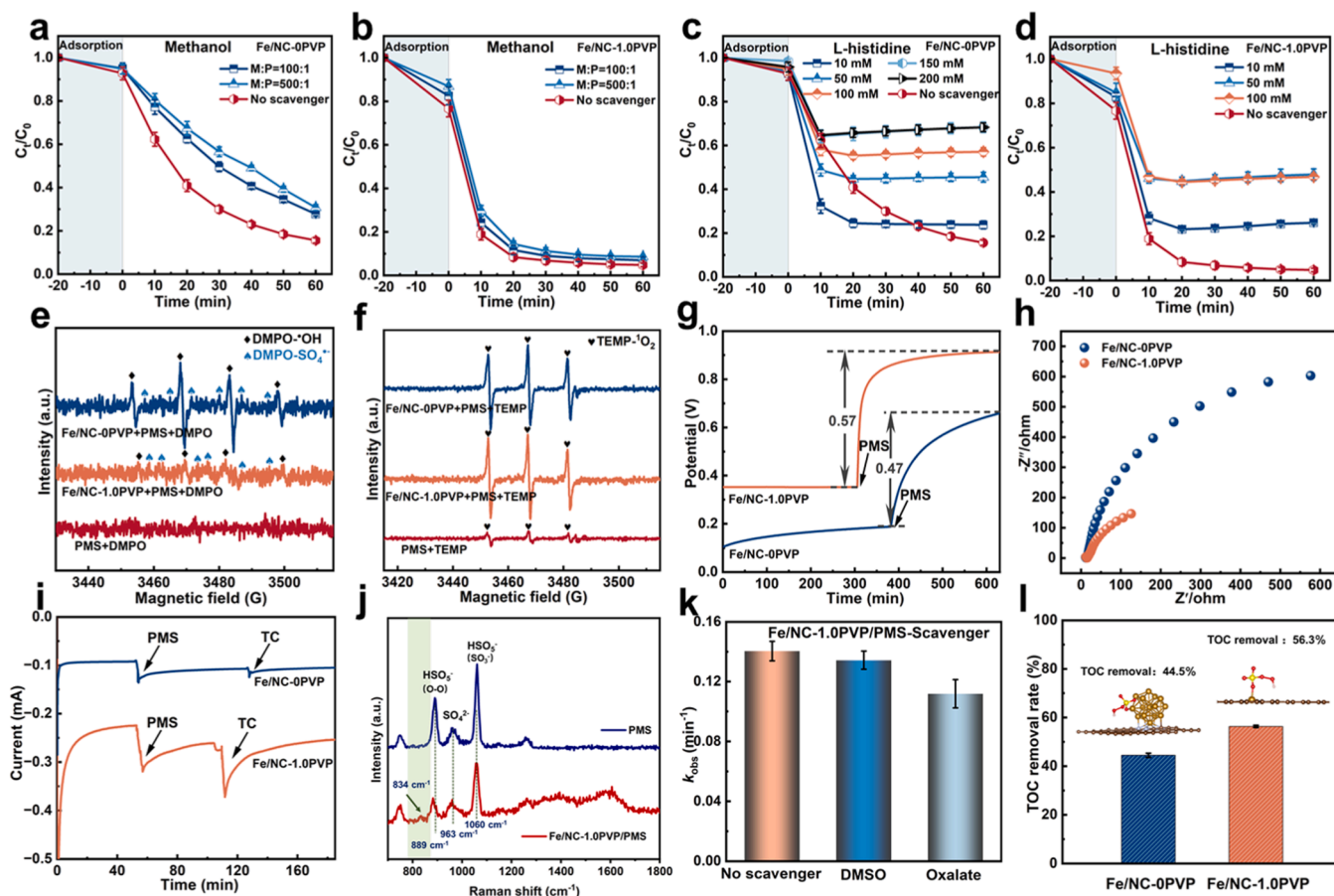

Fig. 3. The effects of different quenchers on TC degradation in Fe/NC-0PVP/PMS and Fe/NC-1.0PVP/PMS systems: (a, b) methanol (M represents methanol and P represents PMS), (c, d) L-histidine; (e) DMPO and (f) TEMP trapped EPR spectra for PMS activation by Fe/NC-0PVP and Fe/NC-1.0PVP. The investigation of electron transfer mechanism: (g) open circuit potential; (h) EIS Nyquist plots of Fe/NC-0PVP and Fe/NC-1.0PVP; (i) *i-t* curves obtained at 0 V vs. Ag/AgCl using 100 mM of Na$_2$SO$_4$ as electrolyte; (j) In-situ Raman spectra of PMS and Fe/NC-1.0PVP/PMS; (k) identification of HV-Fe in Fe/NC-1.0PVP/PMS system; (l) TOC removal rate in Fe/NC-0PVP/PMS and Fe/NC-1.0PVP/PMS systems.

of MeOH (Fig. 3a), suggesting that $SO_4\bullet^-$ and $HO\bullet$ are generated when Fe/NC-0PVP is employed to activate PMS. In contrast, TC removal in Fe/NC-1.0PVP/PMS system is not inhibited by addition of MeOH even though the ratio of MeOH: PMS is increased to 500: 1 (Fig. 3b). Therefore, the contribution of $SO_4\bullet^-$ and $HO\bullet$ to TC removal in Fe/NC-1.0PVP/PMS system can be excluded. EPR spectra are conducted to detect $SO_4\bullet^-$ and $HO\bullet$ using 5,5-dimethyl-1-pyrroline N-oxide (DMPO) as a trapping agent [51]. As shown in Fig. 3e, no obvious signals are obtained in PMS/DMPO system because the self-decomposition of PMS is very weak in the absence of catalyst. The characteristic peaks of DMPO-HO• and DMPO-$SO_4\bullet^-$ adducts are clearly identified in Fe/NC-0PVP/PMS/DMPO system, manifesting that $SO_4\bullet^-$ and $HO\bullet$ are generated through the activation of PMS by Fe/NC-0PVP. However, these typical peaks are almost indistinguishable in Fe/NC-1.0PVP/PMS/DMPO system, eliminating the existence of radicals in the current system. Chloroform (CF) is utilized to evaluate the effect of $O_2\bullet^-$ on TC degradation efficiency [52]. TC degradation in Fe/NC-0PVP/PMS system is slightly inhibited from 84.4 % to 79.7 % by 200 mM of CF, indicating that small amounts of $O_2\bullet^-$ are involved in Fe/NC-0PVP/PMS system (Fig. S20a). The addition of CF exhibits negligible effect on TC removal in Fe/NC-1.0PVP/PMS system, thus excluding the contribution of $O_2\bullet^-$ to TC degradation (Fig. S20b). From the above analysis, it can be identified that the production of active species in PMS activation reaction is linked to the sizes and electronic structures of Fe active centers on the surface of Fe/NC-XPVP.

3.3.2. Identification of non-radical process

L-histidine (L-his) is a typical trapping agent for $^1O_2$ [41]. In Fig. 3c, the degradation efficiency of TC in Fe/NC-0PVP/PMS system is dramatically suppressed from 84.4 % to 31.7 % in the presence of 150 mM of L-his, indicating the critical role of $^1O_2$ in the removal of TC. Of note is that the addition of L-his in Fe/NC-0PVP/PMS system can improve the degradation rate of TC in the first 10 min of the reaction. This may be because L-his can accelerate the decomposition of PMS ($k = 0.197$ $M^{-1}\cdot s^{-1}$) and improve the production of $SO_4\bullet^-$ and $HO\bullet$ [53]. The removal efficiency of TC decreases from 100.0 % to 73.9 % and 52.0 % in the presence of 10 mM and 50 mM of L-his in Fe/NC-1.0PVP/PMS system (Fig. 3d). Moreover, TC degradation cannot be further suppressed when the concentration of L-his is increased to 100 mM. Combined with MeOH quenching experiments, it can be concluded that other non-radical processes are also involved in TC degradation in Fe/NC-1.0PVP/PMS system. EPR spectra with 2,2,6,6-tetramethyl-4-piperidinyloxyl (TEMP) as a capture agent are applied to get more proofs for the contribution of $^1O_2$ to TC removal, as shown in Fig. 3f. The self-decomposition of PMS can produce small amounts of $^1O_2$. Therefore, the three-line peaks with an intensity ratio of 1:1:1 are detected in PMS/TEMP system. The intensity of TEMP-$^1O_2$ signals in Fe/NC-0PVP/PMS/TEMP and Fe/NC-1.0PVP/PMS/TEMP systems is strengthened in the presence of catalyst, manifesting that abundant $^1O_2$ are generated. To sum up, the degradation of TC by Fe/NC-0PVP is realized through the cooperation of radical and non-radical pathways. However, the radical process is almost completely inhibited when the main active centers on the surface of catalyst change from Fe particles to atomically dispersed Fe sites.

Electron transfer mechanism has been widely investigated as an emerging non-radical pathway in PMS-AOTs [54,55]. During the oxidation reaction, electrons can be transferred from pollutants to PMS molecules or intermediate catalyst/PMS* complexes directly to achieve rapid decomposition of organics. Herein, the electron transfer process in Fe/NC-0PVP/PMS and Fe/NC-1.0PVP/PMS systems is investigated by open-circuit potential, electrochemical impedance spectroscopy (EIS), and chronoamperometry test (*i-t* test). As shown in Fig. 3g, the open-circuit potential of electrode coated with Fe/NC-1.0PVP is significantly increased from 0.36 V to 0.93 V when PMS is added into the solution, which means that some intermediate species with higher oxidation ability are produced on the surface of electrode [56]. A

relatively weak potential variation is also detected in Fe/NC-0PVP/PMS system, demonstrating the similar interaction between Fe/NC-0PVP and PMS. Higher potential change in Fe/NC-1.0PVP/PMS system manifests higher adsorption capacity of PMS on the surface of Fe/NC-1.0PVP, which is beneficial to accelerating the mass transfer between PMS and catalyst. The nyquist diagram of Fe/NC-1.0PVP presents a smaller semicircle diameter than that of Fe/NC-0PVP (Fig. 3h), illustrating a smaller charge transfer resistance and easier electron transfer process on Fe/NC-1.0PVP [57]. The instantaneous changes of current density are recorded by *i-t* test, as presented in Fig. 3i. The remarkable current signal is recorded after adding PMS into Fe/NC-1.0PVP system. It means that the electron transfer occurs between catalyst and oxidant, resulting in the generation of intermediate Fe/NC-1.0PVP/PMS* complexes [58]. In-situ Raman spectroscopy is utilized to confirm the formation of Fe/NC-1.0PVP/PMS*, as shown in Fig. 3j. The signals at about 1060 cm^{-1}, 963 cm^{-1}, and 889 cm^{-1} are attributed to HSO_5^-, SO_4^{2-} and HSO_5^- of PMS. The peak intensity of PMS weakens with the addition of Fe/NC-1.0PVP, suggesting a rapid consumption of PMS in the reaction system [59,60]. A newly formed signal at about 834 cm^{-1} is captured in Fe/NC-1.0PVP/PMS system, which is ascribed to the generation of peroxo species (PMS*) bonded to Fe-N_4 sites on the surface of catalyst. At the same time, the peak corresponding to HSO_5^- displays a slight shift from 889 cm^{-1} to 884 cm^{-1}, which implies that PMS molecules can attach to the active Fe-N_4 sites by inner-sphere complexation to form Fe/NC-0PVP/PMS* complexes during the oxidation reaction. When TC is subsequently added in above system, the stronger current response suggests that the electron transfer process between the electron acceptor (Fe/NC-1.0PVP/PMS* complexes) and electron donor (TC) is accelerated. The rapid electron transfer is responsible for efficient TC decomposition in the current system. Although the addition of PMS to Fe/NC-0PVP system also induces a weak current change, the subsequent participation of TC cannot trigger significant current response, indicating that the electron transfer process in Fe/NC-0PVP/PMS system is very weak. PMS molecules adsorbed on the surface of Fe/NC-0PVP are easily activated and decomposed to produce active radicals for TC degradation.

The presence of Fe-N moieties in N-doped carbon usually induces the generation of high-valent iron-oxo species (HV-Fe), which can remove pollutants via a non-radical pathway [46]. Dimethyl sulfoxide (DMSO) can be oxidized by HV-Fe to generate dimethyl sulfone ($DMSO_2$) through an oxygen atom transfer reaction [61]. The consumption of HV-Fe will lead to the depression of pollutant degradation in HV-Fe dominated system. As shown in Fig. S20a, the degradation efficiency of TC in Fe/NC-0PVP/PMS system is improved by addition of DMSO (2 mM), reflecting the absence of HV-Fe. The promotion effect may be due to the fact that Fe particles in Fe/NC-0PVP are corroded by DMSO to generate high concentrations of Fe^{2+}/Fe^{3+} species on the surface of Fe/NC-0PVP for accelerating the oxidation reaction. The removal of TC by Fe/NC-1.0PVP is not influenced by the participation of DMSO (Figs. 3k and S20b), indicating that the contribution of HV-Fe to TC degradation in Fe/NC-1.0PVP/PMS system can also be excluded. Additionally, oxalate is employed as probe for HV-Fe in Fe/NC-1.0PVP/PMS system because the active Fe centers on the catalyst surface are inclined to coordinate with carboxyl groups of oxalate, resulting in the stagnation of TC degradation (Fig. 3k) [62]. The addition of oxalate has no impact on the degradation rates of TC in Fe/NC-1.0PVP/PMS system, further confirming that HV-Fe is not involved in the catalytic process. The quenching experiments and electrochemical tests reveal that the promoted degradation of TC by Fe/NC-1.0PVP is achieved by a completely non-radical pathway ($^1O_2$ and electron transfer process). The switching of reaction mechanism is mainly attributed to the size effect of Fe active centers and the formation of Fe-N_4 configuration in Fe/NC-1.0PVP. The removal efficiency of total organic carbon (TOC) in Fe/NC-1.0PVP/PMS system is 56.3 %, which is higher than that in the Fe/NC-0PVP/PMS system (44.5 %) (Fig. 3l), suggesting that the non-radical oxidation is more favorable to the final decomposition and mineralization of

pollutants in PMS-AOTs.

3.4. Evaluation of practical application performance of catalyst

The practical application performance of catalyst needs to be evaluated from many aspects, for example, the resistance to co-existing anions, general applicability to different pollutants, reusability, and adaptability to complex water environments and so on. Therefore, the degradation efficiency of TC in Fe/NC-1.0PVP/PMS system under different reaction conditions is investigated. As shown in Fig. 4a, the degradation rate of TC is promoted slightly by increasing the catalyst dosage, which is ascribed to the fact that more catalyst can provide more active sites for PMS attachment and facilitate the electron transport, thus improving the degradation efficiency of TC. Additionally, the catalytic activity of Fe/NC-1.0PVP for TC removal is not influenced significantly by changing PMS dosage from 10 mg to 70 mg, revealing high utilization of PMS in the current system (Fig. 4b). From the perspective of economic benefit and degradation efficiency, 5 mg of Fe/NC-1.0PVP and 50 mg of PMS are set as the optimal reaction conditions for other catalytic experiments. Fig. 4c shows the effect of different pH conditions on TC degradation in the Fe/NC-1.0PVP/PMS system. Fe/NC-1.0PVP

exhibits excellent performance in a wide pH range from 1.9 to 10.8. The adsorption capacity of Fe/NC-1.0PVP for TC decreases slightly when the pH values are located in the range of 1.9–3.7 and 9.4–10.8. This may be attributed to the consumption of active sites by intermediate by-products generated under strong acid or base conditions [63]. When PMS is added to the system, the degradation efficiency of TC increases from 81.7 % to 92.1 % in 10 min with the increase of pH value from 1.9 to 10.8, suggesting that neutral and alkaline environments are more conducive to TC degradation in Fe/NC-1.0PVP/PMS system. This is because the enhanced electrostatic adsorption between the catalyst and PMS has a positive effect on PMS activation when pH changes from 6.0 to 10.8 [64]. The outstanding applicability of Fe/NC-1.0PVP to different pH values is of great significance for its application in water remediation. Reaction temperature is one of the important factors affecting the degradation rate of pollutants. As shown in Fig. 4d, the degradation of TC is accelerated by elevating the reaction temperature from 15 °C to 45 °C. The corresponding reaction rate constants are calculated to be 0.1510 min^{-1}, 0.2542 min^{-1}, 0.3431 min^{-1}, and 0.3648 min^{-1}, respectively (Fig. S21). The reaction activation energy (E_a) is fitted to be 25.2 kJ mol^{-1} (Fig. 4e) according to Arrhenius equation (Eq. 3). The relatively low E_a suggests a low thermodynamic
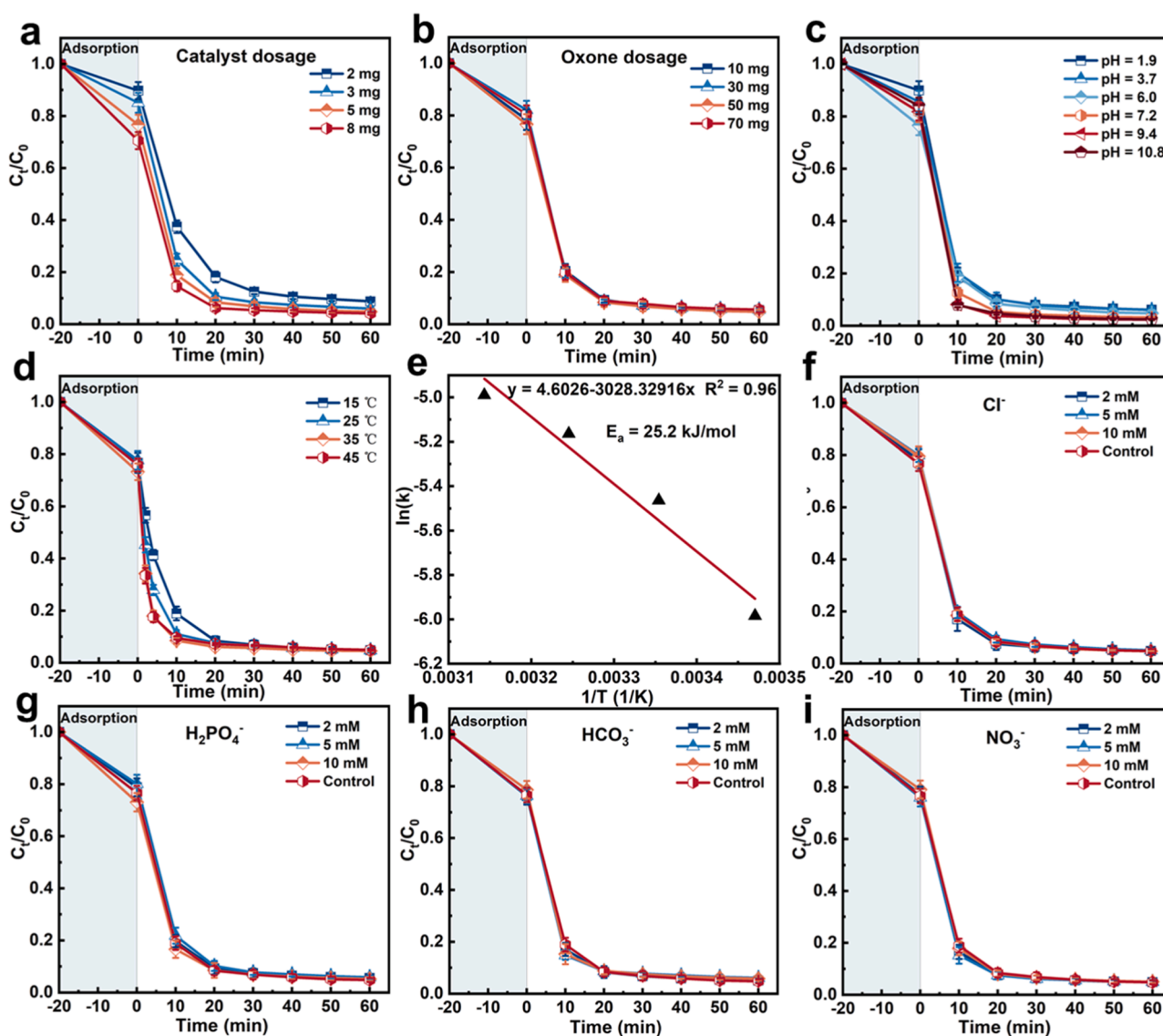

Fig. 4. Influences of (a) catalyst dosage, (b) PMS concentration, (c) initial pH, (d) reaction temperature, (f) Cl$^-$, (g) H$_2$PO$_4^-$, (h) HCO$_3^-$, and (i) NO$_3^-$ on the degradation of TC in Fe/NC-1.0PVP/PMS system; (e) Arrhenius plots on TC degradation and the fitting of activation energy over Fe/NC-1.0PVP.

energy barrier for PMS activation by Fe/NC-1.0PVP [56].

Various inorganic anions commonly found in wastewater can compete with pollutants to consume reactive species, thus weakening the catalytic activity of catalysts [65]. Therefore, some co-existing anions, such as Cl^-, $H_2PO_4^-$, HCO_3^-, and NO_3^-, are employed to evaluate the catalytic performance of Fe/NC-1.0PVP, as displayed in Fig. 4f-i. It can be surprisingly found that different concentrations of these anions make no difference to TC degradation, which indicates that Fe/NC-1.0PVP/PMS system exhibits excellent anti-interference ability to different anions. In view of this, the degradation efficiency of TC in several real water bodies is also investigated (Fig. S22). Notably, Fe/NC-1.0PVP can motivate PMS to completely remove TC in lake water and tap water within 60 min, further reflecting the practical application value of Fe/NC-1.0PVP. The concentration of contaminant has a certain effect on the catalytic ability of catalyst. As indicated in Fig. S23, the adsorption capacity of Fe/NC-1.0PVP for TC decreases gradually with the increase of TC concentration from 10 mg/L to 100 mg/L. However, Fe/NC-1.0PVP can still remove 100 mg/L of TC completely within 60 min. Different types of contaminants including Rhodamine B (RhB), sulfamethoxazole (SMX), and p-nitrophenol (p-NP) are utilized as model pollutants to evaluate the universal applicability of Fe/NC-1.0PVP (Fig. S24). Fe/NC-1.0PVP/PMS system displays considerable degradation performance for p-NP and RhB, and more than 80.0 % of SMX can also be removed within 60 min, suggesting that Fe/NC-1.0PVP can maintain extraordinary catalytic activity in different wastewater environments.

N-doped carbon-based catalysts usually suffer from poor catalytic stability in PMS activation reaction because of the loss or reconstruction of N species, over oxidation of carbon surface, as well as the coverage of active sites by some intermediate products [66]. The stability of Fe/NC-1.0PVP in TC degradation is analyzed by three consecutive runs under the same conditions (Fig. S25). The degradation efficiency of TC after three cycles can still reach 77.3 %. The used catalyst is treated at 300 °C for 2 h for performance revival, and the removal efficiency of TC by the treated catalyst is increased to 89.0 % within 60 min. This result indicates that the deactivation of the catalyst is partly due to the coverage of active sites by intermediate products. To further determine the reason for the performance stagnation of catalyst and investigate TC degradation mechanism, high-resolution XPS spectra of Fe 2p and N 1 s of the fresh and used Fe/NC-1.0PVP are provided (Fig. S26). It can be obviously found that the total Fe content on the catalyst surface decreases from 0.89 % to 0.48 % after the reaction (Table S9). In addition to unavoidable loss of active sites, the decreased Fe content is closely related to the coverage effect of degradation intermediates on the surface of Fe/NC-1.0PVP. The content of O increases dramatically from 4.28 % to 19.85 %, indicating that the oxygen-containing intermediates generated in the oxidation reaction can interact with Fe species and block the Fe-N_4 sites on the surface of catalyst. Moreover, the content ratio of Fe^{2+} decreases from 53.71 % for the fresh Fe/NC-1.0PVP to 36.86 %, and the proportion of Fe^{3+} increases from 46.29 % to 63.14 %. It confirms that Fe^{2+} is oxidized to Fe^{3+} during the oxidation reaction. N 1 s XPS spectra of Fe/NC-1.0PVP before and after reaction reveal that the concentration of Fe-N_4 sites on the surface of catalyst presents a decline from 13.12 % to 10.43 %. Accordingly, the proportion of pyridinic N also decreases significantly from 35.28 % to 20.58 % under the strong oxidation reaction. The overall phenomenon confirms that the Fe-N_4 (pyridinic N) sites are the dominant active centers for the decomposition of TC in the Fe/NC-1.0PVP/PMS system.

3.5. TC degradation pathways

Although satisfactory TC degradation efficiency has been achieved in Fe/NC-1.0PVP/PMS system, the total organic carbon (TOC) removal rate is only 56.3 %. This is because some TC molecules are decomposed into other intermediates instead of being mineralized into carbon dioxide and water. To determine the possible degradation pathway of TC,

LC-MS is utilized to detect the intermediates generated during the degradation process. Eleven main intermediates are identified and presented in Fig. S27 and Table S10. By analyzing these substances, four degradation pathways for TC are proposed accordingly (Fig. 5). Firstly, TC is attacked by $^1O_2$ and electron transfer in Fe/NC-1.0PVP/PMS system and decomposed into smaller intermediates through deamidation, deamination, demethylation, dehydroxylation, ring-opening and oxidation processes [67]. Specifically, for pathway 1, P1 ($m/z = 344$) is mainly derived from the cooperation of dehydroxylation, deamidation, deamination, and oxidation of TC molecules. Subsequently, P1 is further transformed to P2 ($m/z = 192$) through dehydroxylation and ring-opening reactions. In pathway 2, the benzene ring, double bond, and C-N bond of TC may be successively attacked by $^1O_2$ and electron transfer process, resulting in the decomposition of TC into P3 ($m/z = 309$). Then, P3 is decomposed into P4 ($m/z = 214$) after the deamination, decarbonylation, ring-opening and oxidation reactions. In pathway 3, TC loses its dimethylamino groups and undergoes dehydroxylation and ring-opening reactions to form P5 ($m/z = 388$) [56]. Afterwards, P5 goes through a series of ring-opening, demethylation, and methylation reactions to produce P6 ($m/z = 284$). In pathway 4, TC loses the hydroxyl and amide groups, and then undergoes methylation reaction to form P7 ($m/z = 397$). Then, P7 is converted to P8 ($m/z = 240$) through deamination, dehydroxylation, ring-opening, and decarbonylation reactions. The initial decomposition reaction of TC is very fast, and the aforementioned intermediate products will be further decomposed and oxidized into smaller molecules, such as P9 ($m/z = 124$), P10 ($m/z = 60$), and P11 ($m/z = 74$) through the ring-opening steps. Ultimately, part of intermediates are mineralized to CO_2, H_2O and other environmentally friendly species.

3.6. Density functional theory (DFT) calculations

DFT calculations are further performed to give insights into the electron transfer process in Fe/NC-0PVP/PMS and Fe/NC-1.0PVP/PMS systems. All structure models are constructed according to the characterization results. Although the presence of Fe nanoparticles/clusters on carbon matrix can optimize the catalytic activity of Fe/NC-1.0PVP to some extent, the highly dispersed atomic Fe sites (Fe-N_4) are still the main factor determining the rapid decomposition of TC in Fe/NC-1.0PVP/PMS system. Therefore, the optimized configuration structures of Fe/NC-0PVP and Fe/NC-1.0PVP are established in Fig. 6a. In addition, the top and side views of the optimal structure models of PMS adsorbed on the surface of Fe/NC-0PVP and Fe/NC-1.0PVP are also provided. It can be found that the bond length of O-O (l_{o-o}) in PMS molecule is slightly elongated from 1.480 Å to 1.525 Å and 1.509 Å when PMS is adsorbed on the surface of Fe/NC-1.0PVP and Fe/NC-0PVP. The slightly higher l_{o-o} of PMS on the surface of Fe/NC-1.0PVP suggests that the interaction between Fe/NC-1.0PVP and PMS is stronger than that of Fe/NC-0PVP. The electron density differences of PMS adsorbed on Fe/NC-0PVP and Fe/NC-1.0PVP exhibit the distribution of electrons around the two configurations (Fig. 6b). The yellow area represents electron aggregation and the blue area stands for charge depletion. Apparently, for Fe/NC-1.0PVP/PMS system, the charge accumulation region is located on O atoms of PMS, while the charge depletion occurs around Fe-N_4 sites in carbon frameworks. This situation illustrates the occurrence of electron migration from Fe/NC-1.0PVP to PMS. In contrast, no obvious electron transfer from Fe nanoparticles to PMS is observed in Fe/NC-0PVP/PMS system, indicating that PMS on the surface of Fe/NC-0PVP is more likely to be activated to generate active species during the oxidation reaction rather than forming Fe/NC-0PVP/PMS* complexes. Moreover, the adsorption energy (E_{ads}) of PMS on the surface of Fe/NC-1.0PVP is − 1.35 eV, which is almost 2.3 times that of Fe/NC-0PVP ($E_{ads} = -0.59$ eV), indicating a strong and stable interaction between Fe single sites and PMS molecules (Fig. 6c and d). High adsorption energy of Fe/NC-1.0PVP for PMS is conducive to promoting the formation of Fe/NC-1.0PVP/PMS* complexes with strong
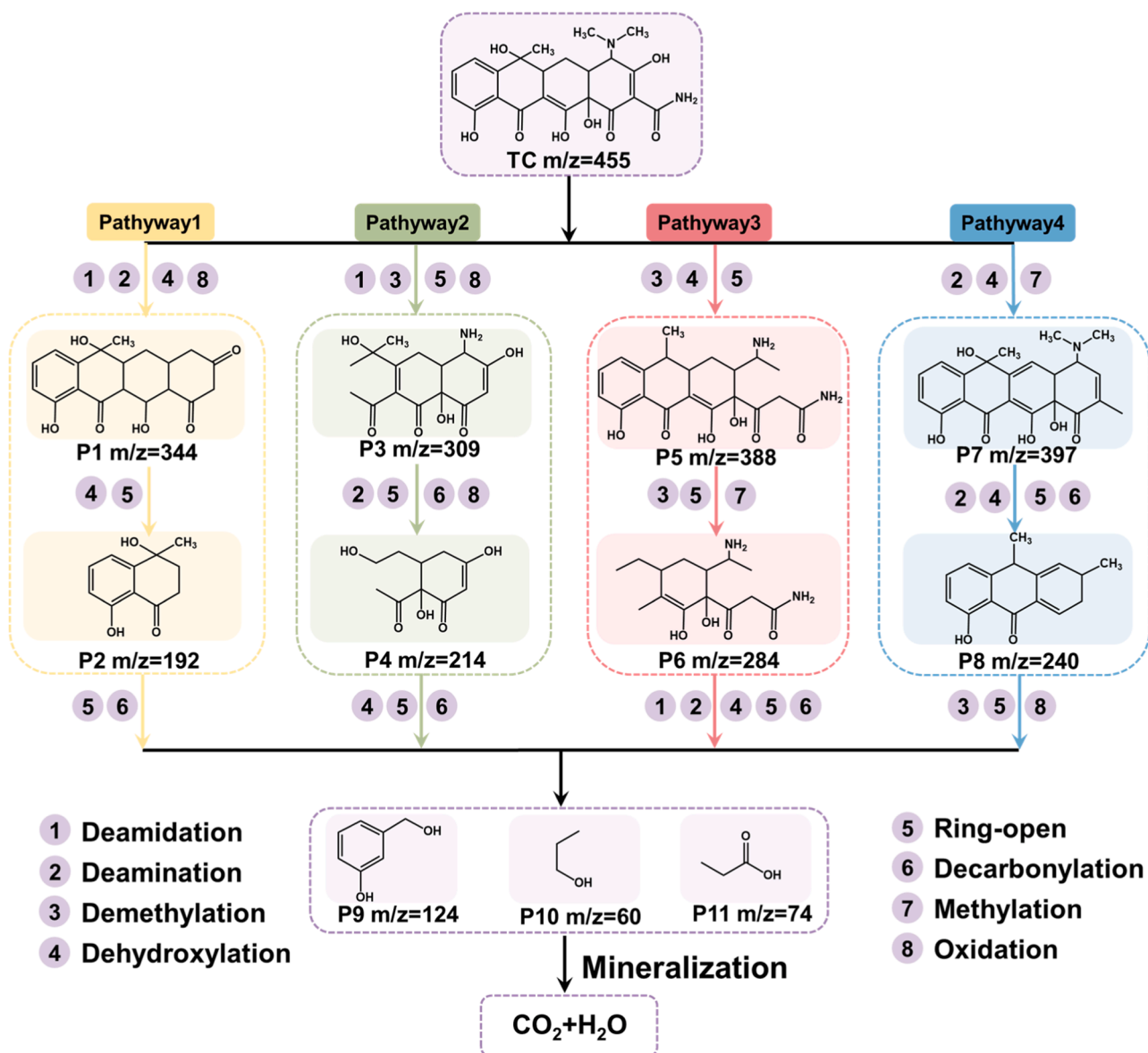
Fig. 5. The proposed degradation pathways of TC in Fe/NC-1.0PVP/PMS system.

oxidation capacity and triggering the electron transfer process from TC to Fe/NC-1.0PVP/PMS* complexes, thus achieving highly efficient degradation of TC [60]. Based on the above analysis, the proposed reaction mechanism switching and possible TC degradation routes in Fe/NC-0PVP/PMS and Fe/NC-1.0PVP/PMS systems are established in Fig. 6e. The scale of Fe active sites on N-doped carbon substrate is flexibly regulated by varying the dosage of PVP in the precursor. Both Fe/NC-0PVP and Fe/NC-1.0PVP can effectively activate PMS to degrade TC. However, the size-dependent catalytic behavior of Fe active sites is observed in two systems. The decrease of Fe active center sizes lead to the switching of reaction mechanism from radical and non-radical oxidation to complete non-radical oxidation. $^1O_2$ and electron transfer process are confirmed to be responsible for the degradation of TC in Fe/NC-1.0PVP/PMS system.

4. Conclusion

The present work develops a simple method to fabricate Fe-based N-doped carbon catalysts (Fe/NC-XPVP) with variable-sized Fe active centers (from particles to single stoms) by pyrolyzing a homogeneous mixture composed of $Fe(NO_3)_3$•9 H_2O, melamine, and PVP. The one-step and solvent-free strategy greatly simplifies the synthesis procedure and reduces the production cost of SACs. PVP plays a crucial role in reducing the size of Fe centers and stabilizing the morphology of carbon substrates. The size-dependent catalytic performance of Fe/NC-XPVP in PMS activation reaction suggests that downsizing Fe particles to atomic level leads to performance improvement and reaction mechanism conversion from radical and non-radical process to complete non-radical process. Moreover, the appropriate co-existence of Fe nanoparticles/clusters and single atoms can optimize the catalytic performance of catalyst to some extent. ROSs analysis and electrochemical tests illustrate that $^1O_2$ and electron transfer dominate the degradation of TC over the atomically dispersed Fe sites (Fe-N$_4$). DFT calculations show that the strong adsorption of PMS on Fe-N$_4$ sites plays a critical role in promoting the formation of intermediate catalyst/PMS* complexes and inducing the occurrence of electron transfer during PMS activation. The Fe-N$_4$/PMS combination exhibits great resistance to complex water environments. The degradation pathway of TC is proposed. This work develops a promising strategy for the precise design and regulation of metal active sites on N-doped carbon and induces selective generation of active
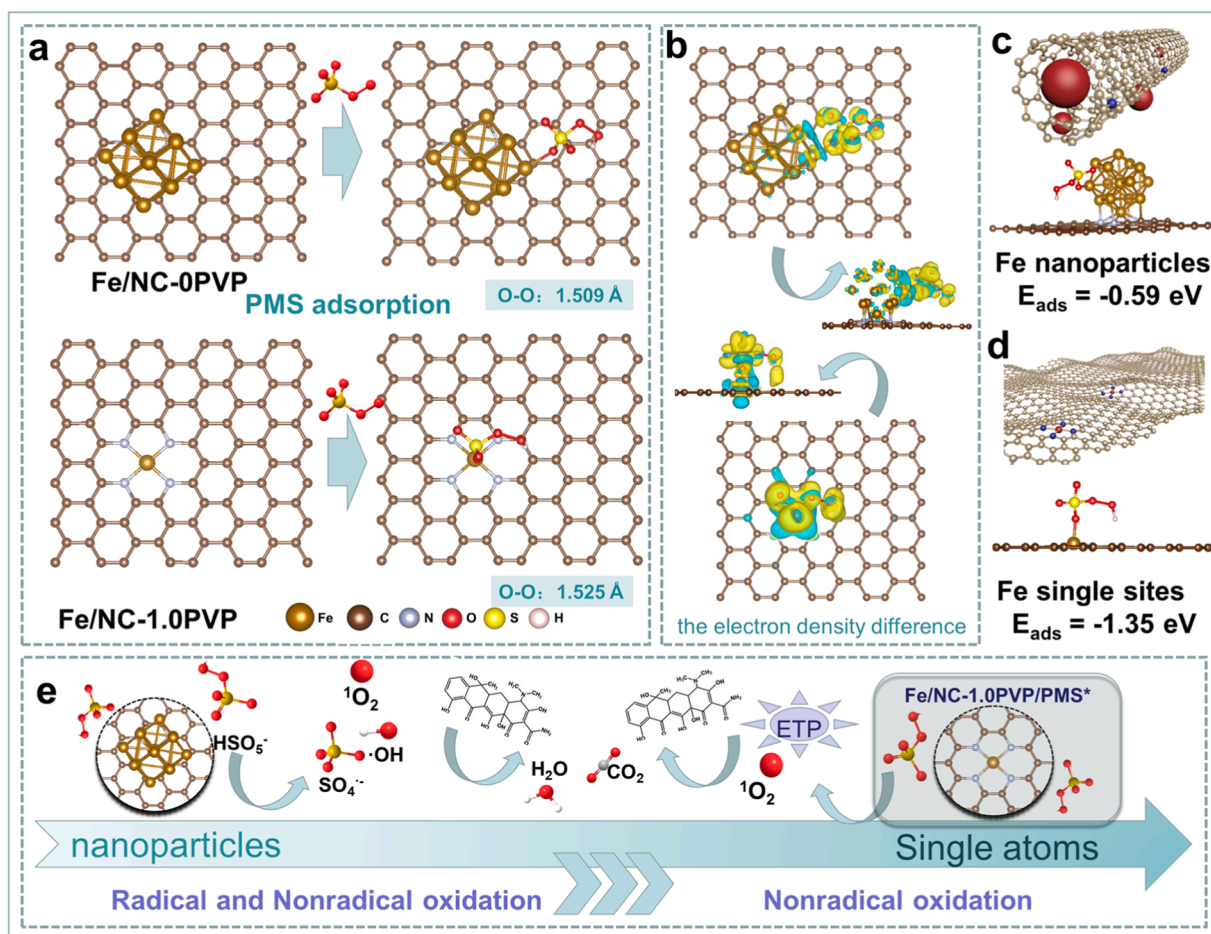
Fig. 6. DFT calculations: (a) the optimized structure and the adsorption geometric configuration of PMS on the surface of Fe/NC-0PVP and Fe/NC-1.0PVP; (b) the charge density differences of Fe/NC-0PVP and Fe/NC-1.0PVP; (c and d) the adsorption energy of PMS on Fe/NC-0PVP and Fe/NC-1.0PVP configuration; (e) the proposed TC degradation mechanism in Fe/NC-1.0PVP/PMS system.

species in PMS-AOTs.

CRediT authorship contribution statement

Haoyue Li: Synthesis, Characterization, Investigation, Data analysis, Writing – original draft. **Na Wang:** Writing – original draft & Modification, Resources, Supervision, Conceptualization, Funding acquistion. **Han Li:** Visualization, Formal analysis. **Ziqiu Ren:** Supervision, Formal analysis, Funding acquistion. **Wenjie Ma:** Supervision, Formal analysis. **Jun Li:** Supervision, Formal analysis. **Yunchen Du:** Supervision, Formal analysis. **Qun Xu:** Visualization, Supervision, Resources.

Declaration of Competing Interest

The authors declare that they have no known competing financial interests or personal relationships that could have appeared to influence the work reported in this paper.

Data availability

Data will be made available on request.

Acknowledgements

Appendix A. Supporting information

Supplementary data associated with this article can be found in the online version at doi:10.1016/j.apcatb.2023.123323.

References

[1] J. Sharma, I.M. Mishra, D.D. Dionysiou, V. Kumar, Oxidative removal of Bisphenol A by UV-C/peroxymonosulfate (PMS): kinetics, influence of co-existing chemicals and degradation pathway, Chem. Eng. J. 276 (2015) 193–204, https://doi.org/10.1016/j.cej.2015.04.021.

[2] M.C. Dlamini, M.S. Maubane-Nkadimeng, J.A. Moma, The use of TiO_2/clay heterostructures in the photocatalytic remediation of water containing organic pollutants: a review, J. Environ. Chem. Eng. 9 (2021), 106546, https://doi.org/10.1016/j.jece.2021.106546.

[3] Y.A. Lim, M.N. Chong, S.C. Foo, I.M.S.K. Ilankoon, Analysis of direct and indirect quantification methods of CO_2 fixation via microalgae cultivation in photobioreactors: a critical review, Renew. Sustain. Energy Rev. 137 (2021), 110579, https://doi.org/10.1016/j.rser.2020.110579.

[4] P. Hu, M. Long, Cobalt-catalyzed sulfate radical-based advanced oxidation: a review on heterogeneous catalysts and applications, Appl. Catal. B Environ. 181 (2016) 103–117, https://doi.org/10.1016/j.apcatb.2015.07.024.

[5] N. Wang, W.J. Ma, Z.Q. Ren, Y.C. Du, P. Xu, X.J. Han, Prussian blue analogues derived porous nitrogen-doped carbon microspheres as high-performance metal-free peroxymonosulfate activators for non-radical-dominated degradation of organic pollutants, J. Mater. Chem. A. 6 (2018) 884–895, https://doi.org/10.1039/c7ta08472b.

[6] W.D. Oh, Z.L. Dong, T.T. Lim, Generation of sulfate radical through heterogeneous catalysis for organic contaminants removal: current development, challenges and prospects, Appl. Catal. B Environ. 194 (2016) 169–201, https://doi.org/10.1016/j.apcatb.2016.04.003.

[7] S. Giannakis, K.Y.A. Lin, F. Ghanbari, A review of the recent advances on the treatment of industrial wastewaters by Sulfate Radical-based Advanced Oxidation Processes (SR-AOPs), Chem. Eng. J. 406 (2021), 127083, https://doi.org/10.1016/j.cej.2020.127083.

[8] J.L. Wang, S.Z. Wang, Effect of inorganic anions on the performance of advanced oxidation processes for degradation of organic contaminants, Chem. Eng. J. 411 (2021), 128392, https://doi.org/10.1016/j.cej.2020.128392.

[9] S.Z. Wang, H.Y. Liu, J.L. Wang, Nitrogen, sulfur and oxygen co-doped carbon-armored Co/Co$_9$S$_8$ rods (Co/Co$_9$S$_8$@N-S-O-C) as efficient activator of peroxymonosulfate for sulfamethoxazole degradation, J. Hazard. Mater. 387 (2020), 121669, https://doi.org/10.1016/j.jhazmat.2019.121669.

[10] Z.Y. Feng, Q.L. Tian, Q.Q. Yang, Y.B. Zhou, H.Y. Zhao, G.H. Zhao, Selectively photoelectrocatalytic reduction of oxygen to hydroxyl radical and singlet oxygen: mechanism and validation in coal wastewater, Appl. Catal. B Environ. 286 (2021), 119908, https://doi.org/10.1016/j.apcatb.2021.119908.

[11] F. Chen, L.L. Liu, J.J. Chen, W.W. Li, Y.P. Chen, Y.J. Zhang, J.H. Wu, S.C. Mei, Q. Yang, H.Q. Yu, Efficient decontamination of organic pollutants under high salinity conditions by a nonradical peroxymonosulfate activation system, Water Res. 191 (2021), 116799, https://doi.org/10.1016/j.watres.2020.116799.

[12] R. Luo, M.Q. Li, C.H. Wang, M. Zhang, M.A.N. Khan, X.Y. Sun, J.Y. Shen, W.Q. Han, L.J. Wang, J.S. Li, Singlet oxygen-dominated non-radical oxidation process for efficient degradation of bisphenol A under high salinity condition, Water Res. 148 (2019) 416–424, https://doi.org/10.1016/j.watres.2018.10.087.

[13] D.H. Li, S.X. Zhang, S.N. Li, J.C. Tang, T. Hua, F.X. Li, Mechanism of the application of single-atom catalyst-activated PMS/PDS to the degradation of organic pollutants in water environment: a review, J. Clean. Prod. 397 (2023), 136468, https://doi.org/10.1016/j.jclepro.2023.136468.

[14] Y.J. Zhang, G.X. Huang, L.R. Winter, J.J. Chen, L. Tian, S.C. Mei, Z. Zhang, F. Chen, Z.Y. Guo, R. Ji, Y.Z. You, W.W. Li, X.W. Liu, H.Q. Yu, M. Elimelech, Simultaneous nanocatalytic surface activation of pollutants and oxidants for highly efficient water decontamination, Nat. Commun. 13 (2022), 3005, https://doi.org/10.1038/s41467-022-30560-9.

[15] R.Y. Chen, X.C. Dou, J.Z. Xia, Y.G. Chen, H.F. Shi, Boosting peroxymonosulfate activation over Bi$_2$MoO$_6$/CuWO$_4$ to rapidly degrade tetracycline: intermediates and mechanism, Sep. Purif. Technol. 296 (2022), 121345, https://doi.org/10.1016/j.seppur.2022.121345.

[16] M. Xie, J.C. Tang, L.S. Kong, W.H. Lu, V. Natarajan, F. Zhu, J.H. Zhan, Cobalt doped g-C$_3$N$_4$ activation of peroxymonosulfate for monochlorophenols degradation, Chem. Eng. J. 360 (2019) 1213–1222, https://doi.org/10.1016/j.cej.2018.10.130.

[17] H.Q. Zhang, R. Lee Smith, H.X. Guo, X.H. Qi, Cobalt cross-linked ordered mesoporous carbon as peroxymonosulfate activator for sulfamethoxazole degradation, Chem. Eng. J. 472 (2023), 145060, https://doi.org/10.1016/j.cej.2023.145060.

[18] L.J. Zhang, B.N. Wang, W.J. Ma, B. Li, Y.L. Liu, Y.C. Du, Fe$_3$C/Fe nanoparticles decorated three-dimensional nitrogen-doped carbon foams for highly efficient bisphenol A removal through peroxymonosulfate activation, Chem. Eng. J. 437 (2022), 135472, https://doi.org/10.1016/j.cej.2022.135472.

[19] F.J. Perez-Alonso, D.N. McCarthy, A. Nierhoff, P. Hernandez-Fernandez, C. Strebel, I.E. Stephens, J.H. Nielsen, I. Chorkendorff, The effect of size on the oxygen electroreduction activity of mass-selected platinum nanoparticles, Angew. Chem. Int. Ed. 124 (2012) 4719–4721, https://doi.org/10.1002/ange.201200586.

[20] W.Y. Chen, J. Ji, X. Feng, X.Z. Duan, G. Qian, P. Li, X.G. Zhou, D. Chen, W.K. Yuan, Mechanistic insight into size-dependent activity and durability in Pt/CNT catalyzed hydrolytic dehydrogenation of ammonia borane, J. Am. Chem. Soc. 136 (2014) 16736–16739, https://doi.org/10.1021/ja509778y.

[21] C.Y. Dong, C. Lian, S.C. Hu, Z.S. Deng, J.Q. Gong, M.D. Li, H.L. Liu, M.Y. Xing, J. L. Zhang, Size-dependent activity and selectivity of carbon dioxide photocatalytic reduction over platinum nanoparticles, Nat. Commun. 9 (2018), 1252, https://doi.org/10.1038/s41467-018-03666-2.

[22] H.W. Wang, X.K. Gu, X.S. Zheng, H.B. Pan, J.F. Zhu, S. Chen, L.N. Cao, W.X. Li, J. L. Lu, Disentangling the size-dependent geometric and electronic effects of palladium nanocatalysts beyond selectivity, Sci. Adv. 5 (2019), eaat6413, https://doi.org/10.1126/sciadv.aat6413.

[23] H.R. Song, R. Du, Y.W. Wang, D.Y. Zu, R. Zhou, Y. Cai, F.X. Wang, Z. Li, Y.M. Shen, C.P. Li, Anchoring single atom cobalt on two-dimensional MXene for activation of peroxymonosulfate, Appl. Catal. B Environ. 286 (2021), 119898, https://doi.org/10.1016/j.apcatb.2021.119898.

[24] H.D. Xu, N. Jiang, D. Wang, L.H. Wang, Y.F. Song, Z.Q. Chen, J. Ma, T. Zhang, Improving PMS oxidation of organic pollutants by single cobalt atom catalyst through hybrid radical and non-radical pathways, Appl. Catal. B Environ. 263 (2020), 118350, https://doi.org/10.1016/j.apcatb.2019.118350.

[25] Y.J. Yao, H.Y. Yin, M.X. Gao, Y. Hu, H.H. Hu, M. Yu, S.B. Wang, Electronic structure modulation of covalent organic frameworks by single-atom Fe doping for enhanced oxidation of aqueous contaminants, Chem. Eng. Sci. 209 (2019), 115211, https://doi.org/10.1016/j.ces.2019.115211.

[26] J.H. Hu, Y.B. Zou, Y. Li, Y.N. Xiao, M. Li, L. Lin, B. Li, X.Y. Li, Efficacy and mechanism of peroxymonosulfate activation by single-atom transition metal catalysts for the oxidation of organic pollutants: Experimental validation and theoretical calculation, J. Colloid Interface Sci. 645 (2023) 1–11, https://doi.org/10.1016/j.jcis.2023.04.093.

[27] Z. Zhou, M.Q. Li, C.G. Kuai, Y.X. Zhang, V.F. Smith, F. Lin, A. Aiello, D.P. Durkin, H.N. Chen, D.M. Shuai, Fe-based single-atom catalysis for oxidizing contaminants of emerging concern by activating peroxides, J. Hazard. Mater. 418 (2021), 126294, https://doi.org/10.1016/j.jhazmat.2021.126294.

[28] P.J. Duan, J.W. Pan, W.Y. Du, Q.Y. Yue, B.Y. Gao, X. Xu, Activation of peroxymonosulfate via mediated electron transfer mechanism on single-atom Fe catalyst for effective organic pollutants removal, Appl. Catal. B Environ. 299 (2021), 120714, https://doi.org/10.1016/j.apcatb.2021.120714.

[29] H. Liu, Y.X. Fu, S.X. Chen, W.C. Zhang, K.S. Xiang, F.H. Shen, R.Y. Xiao, L.Y. Chai, F.P. Zhao, A layered g-C$_3$N$_4$ support Single-Atom Fe-N$_4$ catalyst derived from hemin to activate PMS for selective degradation of electron-rich compounds via singlet oxygen species, Chem. Eng. J. 474 (2023), 145571, https://doi.org/10.1016/j.cej.2023.145571.

[30] Z.Q. Li, K. Li, S.L. Ma, B.J. Dang, Y. Li, H.C. Fu, J.G. Du, Q.X. Meng, Activation of peroxymonosulfate by iron-biochar composites: comparison of nanoscale Fe with single-atom Fe, J. Colloid Interface Sci. 582 (2021) 598–609, https://doi.org/10.1016/j.jcis.2020.08.049.

[31] Y.H. Li, D.Y. Lin, Y.F. Li, P.K. Jiang, X.B. Fang, B. Yu, Nonradical-dominated peroxymonosulfate activation through bimetallic Fe/Mn-loaded hydroxyl-rich biochar for efficient degradation of tetracycline, Nano Res. 16 (2022) 155–165, https://doi.org/10.1007/s12274-022-4640-8.

[32] N. Wang, H.Y. Li, H.J. Wang, H.H. Yang, Z.Q. Ren, R. Xu, Temperature-induced low-coordinate Ni single-atom catalyst for boosted CO$_2$ electroreduction activity, Small (2023), 2301469, https://doi.org/10.1002/smll.202301469.

[33] G. Kresse, J. Furthmuller, Efficiency of ab-initio total energy calculations for metals and semiconductors using a plane-wave basis set, Comput. Mater. Sci. 6 (1996) 15–50, https://doi.org/10.1016/0927-0256(96)00008-0.

[34] J.P. Perdew, K. Burke, M. Ernzerhof, Generalized gradient approximation made simple, Phys. Rev. Lett. 78 (1997) 3865–3868, https://doi.org/10.1103/physrevlett.77.3865.

[35] P.E. Blöchl, Projector augmented-wave method, Phys. Rev. B. 50 (1994) 17953–17979, https://doi.org/10.1103/physrevb.50.17953.

[36] G. Kresse, D. Joubert, From ultrasoft pseudopotentials to the projector augmented-wave method, Phys. Rev. B 59 (1999) 1758–1775, https://doi.org/10.1103/PhysRevB.59.1758.

[37] R. Si, Y.W. Zhang, L.P. You, C.H. Yan, Self-organized monolayer of nanosized ceria colloids stabilized by poly(vinylpyrrolidone), J. Phys. Chem. B 110 (2006) 5994–6000, https://doi.org/10.1021/jp057501x.

[38] K.M. Koczkur, S. Mourdikoudis, L. Polavarapu, S.E. Skrabalak, Polyvinylpyrrolidone (PVP) in nanoparticle synthesis, Dalton Trans. 44 (2015) 17883–17905, https://doi.org/10.1039/c5dt02964c.

[39] Z. Cao, Y.P. Zhao, J.M. Li, Q.Z. Wang, Q. Mei, H.F. Cheng, Rapid electron transfer-promoted tetracycline hydrochloride degradation: enhanced activity in visible light-coupled peroxymonosulfate with PdO/g-C$_3$N$_4$/kaolinite catalyst, Chem. Eng. J. 457 (2023), 141191, https://doi.org/10.1016/j.cej.2022.141191.

[40] L.M. Jin, S.J. You, N.Q. Ren, B. Ding, Y.B. Liu, Mo vacancy-mediated activation of peroxymonosulfate for ultrafast micropollutant removal using an electrified MXene filter functionalized with Fe single atoms, Environ. Sci. Technol. 56 (2022) 11750–11759, https://doi.org/10.1021/acs.est.2c03904.

[41] J.L. Xie, L. Chen, X. Luo, L. Huang, S.Y. Li, X.B. Gong, Degradation of tetracycline hydrochloride through efficient peroxymonosulfate activation by B, N co-doped porous carbon materials derived from metal-organic frameworks: nonradical pathway mechanism, Sep. Purif. Technol. 281 (2022), 119887, https://doi.org/10.1016/j.seppur.2021.119887.

[42] A.C. Ferrari, Raman spectroscopy of graphene and graphite: disorder, electron-phonon coupling, doping and nonadiabatic effects, Solid State Commun. 143 (2007) 47–57, https://doi.org/10.1016/j.ssc.2007.03.052.

[43] K. Zhu, Q. Bin, Y.Q. Shen, J. Huang, D.D. He, W.J. Chen, In-situ formed N-doped bamboo-like carbon nanotubes encapsulated with Fe nanoparticles supported by biochar as highly efficient catalyst for activation of persulfate (PS) toward degradation of organic pollutants, Chem. Eng. J. 402 (2020), 126090, https://doi.org/10.1016/j.cej.2020.126090.

[44] K. Srinivas, Z. Chen, F. Ma, A. Chen, Z.H. Zhang, Y. Wu, M.Q. Zhu, Y.F. Chen, Highly accessible atomically dispersed Fe-N$_x$ sites coupled with Fe$_3$C@C core-shell nanoparticles boost the oxygen catalysis for ultra-stable rechargeable Zn-air batteries, Appl. Catal. B Environ. 335 (2023), 122887, https://doi.org/10.1016/j.apcatb.2023.122887.

[45] H.D. Xu, Y.Q. Sheng, New insights into the degradation of chloramphenicol and fluoroquinolone antibiotics by peroxymonosulfate activated with FeS: performance and mechanism, Chem. Eng. J. 414 (2021), 128823, https://doi.org/10.1016/j.cej.2021.128823.

[46] L.J. Peng, X.G. Duan, Y.N. Shang, B.Y. Gao, X. Xu, Engineered carbon supported single iron atom sites and iron clusters from Fe-rich Enteromorpha for Fenton-like reactions via nonradical pathways, Appl. Catal. B Environ. 287 (2021), 119963, https://doi.org/10.1016/j.apcatb.2021.119963.

[47] L.J. Peng, Y.N. Shang, B.Y. Gao, X. Xu, Co$_3$O$_4$ anchored in N, S heteroatom co-doped porous carbons for degradation of organic contaminant: role of pyridinic N-Co binding and high tolerance of chloride, Appl. Catal. B Environ. 282 (2021), 119484, https://doi.org/10.1016/j.apcatb.2020.119484.

[48] W.H. Ren, X. Tan, C. Jia, A. Krammer, Q. Sun, J.T. Qu, S.C. Smith, A. Schueler, X. L. Hu, C. Zhao, Electronic regulation of nickel single atoms by confined nickel nanoparticles for energy-efficient CO$_2$ electroreduction, Angew. Chem. Int. Ed. 61 (2022), e202203335, https://doi.org/10.1002/anie.202203335.

[49] C. Hou, J. Zhao, L.B. Yang, J.B. Chen, X.F. Xia, X.F. Zhou, Y.L. Zhang, A single-atom Fe-N-C catalyst with superior Fenton-like reaction performance prepared facilely using microalgae: key roles of oxygen and interactions between Fe-N$_x$ and Fe/Fe compounds, Appl. Catal. B Environ. 339 (2023), 123135, https://doi.org/10.1016/j.apcatb.2023.123135.

[50] X. Guo, H. Zhang, Y.Y. Yao, C.M. Xiao, X. Yan, K. Chen, J.W. Qi, Y.J. Zhou, Z. G. Zhu, X.Y. Sun, J.S. Li, Derivatives of two-dimensional MXene-MOFs

heterostructure for boosting peroxymonosulfate activation: Enhanced performance and synergistic mechanism, Appl. Catal. B Environ. 323 (2023), 122136, https://doi.org/10.1016/j.apcatb.2022.122136.

[51] M.J. Xu, J. Li, Y. Yan, X.G. Zhao, J.F. Yan, Y.H. Zhang, B. Lai, X. Chen, L.P. Song, Catalytic degradation of sulfamethoxazole through peroxymonosulfate activated with expanded graphite loaded CoFe$_2$O$_4$ particles, Chem. Eng. J. 369 (2019) 403–413, https://doi.org/10.1016/j.cej.2019.03.075.

[52] H. Zhu, A. Guo, S.M. Wang, Y. Long, G.Y. Fan, X.J. Yu, Efficient tetracycline degradation via peroxymonosulfate activation by magnetic Co/N co-doped biochar: Emphasizing the important role of biochar graphitization, Chem. Eng. J. 450 (2022), 138428, https://doi.org/10.1016/j.cej.2022.138428.

[53] L.W. Gao, Y. Guo, J.H. Zhan, G. Yu, Y.J. Wang, Assessment of the validity of the quenching method for evaluating the role of reactive species in pollutant abatement during the persulfate-based process, Water Res. 221 (2022), 118730, https://doi.org/10.1016/j.watres.2022.118730.

[54] J. Zhang, H.X. Zeng, L.J. Bu, S.Q. Zhou, Z. Shi, L. Deng, Cu^0 incorporated cobalt/nitrogen doped carbonaceous frameworks derived from ZIF-67 (Cu@CoNC) as PMS activator for efficient degradation of naproxen: direct electron transfer and ^{1}O$_2$ dominated nonradical mechanisms, Chem. Eng. J. 454 (2023), 139989, https://doi.org/10.1016/j.cej.2022.139989.

[55] H.R. Song, S.T. Pan, Y.W. Wang, Y. Cai, W. Zhang, Y.M. Shen, C.P. Li, MXene-mediated electron transfer in Cu(II)/PMS process: from Cu(III) to Cu(I), Sep. Purif. Technol. 297 (2022), 121428, https://doi.org/10.1016/j.seppur.2022.121428.

[56] L. Hu, Y.W. Zhang, X.Y. Liu, H. Zhu, J. Wu, Y. Wang, Y. Long, G.Y. Fan, A robust peroxymonosulfate activator for tetracycline degradation: mitigating deactivation via stitching N-doped carbon nanotubes with encapsulated Co nanoparticles in bubble-like architectures, Chem. Eng. J. 450 (2022), 138219, https://doi.org/10.1016/j.cej.2022.138219.

[57] F. Li, T.B. Huang, F.B. Sun, L. Chen, P.S. Li, F. Shao, X.D. Yang, W. Liu, Ferric oxide nanoclusters with low-spin Fe^{III} anchored g-C$_3$N$_4$ rod for boosting photocatalytic activity and degradation of diclofenac in water under solar light, Appl. Catal. B Environ. 317 (2022), 121725, https://doi.org/10.1016/j.apcatb.2022.121725.

[58] W. Ren, L.L. Xiong, X.H. Yuan, Z.W. Yu, H. Zhang, X.G. Duan, S.B. Wang, Activation of peroxydisulfate on carbon nanotubes: electron-transfer mechanism, Environ. Sci. Technol. 53 (2019) 14595–14603, https://doi.org/10.1021/acs.est.9b05475.

[59] Y.Y. Yao, C.H. Wang, Y.P. Yang, S. Zhang, X. Yan, C.M. Xiao, Y.J. Zhou, Z.J. Zhu, J.W. Qi, X.Y. Sun, J.S. Li, Mn-Co dual sites relay activation of peroxymonosulfate for accelerated decontamination, Appl. Catal. B Environ. 330 (2023), 122656, https://doi.org/10.1016/j.apcatb.2023.122656.

[60] K.X. Yin, L.J. Peng, D.D. Chen, S.Y. Liu, Y.J. Zhang, B.Y. Gao, K.F. Fu, Y.N. Shang, X. Xu, High-loading of well dispersed single-atom catalysts derived from Fe-rich marine algae for boosting Fenton-like reaction: role identification of iron center and catalytic mechanisms, Appl. Catal. B Environ. 336 (2023), 122951, https://doi.org/10.1016/j.apcatb.2023.122951.

[61] X.M. Peng, J.Q. Wu, Z.L. Zhao, X. Wang, H.L. Dai, L. Xu, G.P. Xu, Y. Jian, F.P. Hu, Activation of peroxymonosulfate by single-atom Fe-g-C$_3$N$_4$ catalysts for high efficiency degradation of tetracycline via nonradical pathways: role of high-valent iron-oxo species and Fe-N$_x$ sites, Chem. Eng. J. 427 (2022), 130803, https://doi.org/10.1016/j.cej.2021.130803.

[62] C. Zhao, L.H. Meng, H.Y. Chu, J.F. Wang, T.Y. Wang, Y.H. Ma, C.C. Wang, Ultrafast degradation of emerging organic pollutants via activation of peroxymonosulfate over Fe$_3$C/Fe@N-C-x: singlet oxygen evolution and electron-transfer mechanisms, Appl. Catal. B Environ. 321 (2023), 122034, https://doi.org/10.1016/j.apcatb.2022.122034.

[63] X.H. Wang, Z.K. Xiong, H.L. Shi, Z.L. Wu, B.K. Huang, H. Zhang, P. Zhou, Z.C. Pan, W. Liu, B. Lai, Switching the reaction mechanisms and pollutant degradation routes through active center size-dependent Fenton-like catalysis, Appl. Catal. B Environ. 329 (2023), 122569, https://doi.org/10.1016/j.apcatb.2023.122569.

[64] Y.Q. Yu, Y.F. Ji, J.H. Lu, X.M. Yin, Q.S. Zhou, Degradation of sulfamethoxazole by Co$_3$O$_4$-palygorskite composites activated peroxymonosulfate oxidation, Chem. Eng. J. 406 (2021), 126759, https://doi.org/10.1016/j.cej.2020.126759.

[65] X. Guo, Q.C. Zhang, H.W. He, A. Cai, S.B. Xi, J.Q. Du, F.B. Zhang, X.B. Fan, W.C. Peng, Y. Li, Wastewater flocculation substrate derived three-dimensional ordered macroporous Co single-atom catalyst for singlet oxygen-dominated peroxymonosulfate activation, Appl. Catal. B Environ. 335 (2023), 122886, https://doi.org/10.1016/j.apcatb.2023.122886.

[66] Y.L. Liu, F.Y. Wang, B.J. Sun, P. Xu, L.J. Zhang, X.J. Han, Y.C. Du, In situ growth of nitrogen-doped carbon nanotubes based on hierarchical Ni@C microspheres for high efficiency bisphenol A removal through peroxymonosulfate activation, ACS Appl. Mater. Interfaces 14 (2022) 21371–21382, https://doi.org/10.1021/acsami.2c03840.

[67] M.X. Cheng, Y.C. Zhang, B. Lai, L.Z. Wang, S.J. Yang, K.L. Li, D.Q. Wang, Y.G. Wu, G.H. Chen, J. Qian, Nitrogen and phosphorus co-doped porous carbons (NPCs) for peroxydisulfate (PDS) activation towards tetracycline degradation: defects enhanced adsorption and non-radical mechanism dominated by electron transfer, Chem. Eng. J. 455 (2023), 140615, https://doi.org/10.1016/j.cej.2022.140615.